Neuron

Article

Actin- and Myosin-Dependent Vesicle Loading of Presynaptic Docking Sites Prior to Exocytosis

Highlights

- Variance of cumulative vesicle counts during trains is low
- Release statistics suggest two-step replacement site/docking site transition
- Vesicle supply from replacement site depends on actin and myosin II
- Facilitation may reflect enhanced docking site loading from replacement site

Authors

Takafumi Miki, Gerardo Malagon,
Camila Pulido, Isabel Llano,
Erwin Neher, Alain Marty

Correspondence

alain.marty@parisdescartes.fr

In Brief

Miki et al. (2016) analyze statistics of vesicular release at single glutamatergic synapses during action potential trains and suggest that vesicles transit through a replacement site and a docking site before exocytosis, in a process driven by actin and myosin II.

Miki et al., 2016, Neuron *91*, 808–823
August 17, 2016
http://dx.doi.org/10.1016/j.neuron.2016.07.033

CellPress

Neuron
Article

Actin- and Myosin-Dependent Vesicle Loading of Presynaptic Docking Sites Prior to Exocytosis

Takafumi Miki,[1] Gerardo Malagon,[1] Camila Pulido,[1] Isabel Llano,[1] Erwin Neher,[2] and Alain Marty[1],*
[1]Laboratory of Brain Physiology, CNRS UMR 8118, Paris Descartes University, 45 rue des Saints Pères, 75006 Paris, France
[2]Max Planck Institute for Biophysical Chemistry, am Fassberg 11, D37077 Göttingen, Germany
*Correspondence: alain.marty@parisdescartes.fr
http://dx.doi.org/10.1016/j.neuron.2016.07.033

SUMMARY

Variance analysis of postsynaptic current amplitudes suggests the presence of distinct docking sites (also called release sites) where vesicles pause before exocytosis. Docked vesicles participate in the readily releasable pool (RRP), but the relation between docking site number and RRP size remains unclear. It is also unclear whether all vesicles of the RRP are equally release competent, and what cellular mechanisms underlie RRP renewal. We address here these questions at single glutamatergic synapses, counting released vesicles using deconvolution. We find a remarkably low variance of cumulative vesicle counts during action potential trains. This, combined with Monte Carlo simulations, indicates that vesicles transit through two successive states before exocytosis, so that the RRP is up to 2-fold higher than the docking site number. The transition to the second state has a very rapid rate constant, and is specifically inhibited by latrunculin B and blebbistatin, suggesting the involvement of actin and myosin.

INTRODUCTION

The last step of presynaptic signaling, exocytosis, has been extensively studied in central synapses (Schneggenburger and Neher, 2000; Bollmann et al., 2000), but steps immediately preceding exocytosis remain poorly understood. Current views focus on a special set of synaptic vesicles (SVs), the readily releasable pool (RRP), that restricts the number of release events elicited by a sudden stimulus (Zucker et al., 2009). Only SVs in the RRP can be released, so that RRP exhaustion is a major contributor to synaptic depression following repetitive stimulation. Once exhausted, the RRP is replenished from another pool, the recycling pool (Rizzoli and Betz, 2005). The mechanisms governing RRP replenishment are still unclear, apart from the fact that an elevation of cytosolic calcium speeds up this process (Rizzoli and Betz, 2005; Zucker et al., 2009).

Increasing evidence suggests a role of cytoskeletal proteins in RRP recruitment (Hallermann and Silver, 2013). In particular, disrupting actin filaments, or blocking non-muscle myosin II or its regulatory kinase myosin light chain kinase, interferes with RRP recruitment (Mochida et al., 1994; Ryan, 1999; Cole et al., 2000; Takagishi et al., 2005; Hayashida et al., 2015). This suggests an active role of actin and myosin II in supplying SVs to the RRP, although contrasting studies have pointed to an inhibitory role of the same proteins, preventing access to the plasma membrane (Morales et al., 2000; Srinivasan et al., 2008). Alternatively, a scaffolding role, restraining SV diffusion away from the active zone, has been postulated (Sankaranarayanan et al., 2003).

In the calyx of Held and at mossy fiber-granule cell synapses, two distinct components of the RRP can be distinguished when delivering a prolonged presynaptic depolarizing voltage step. In these conditions a fast releasable pool (FRP; about 3 SVs per active zone at calyx synapses) is first released, followed by the release of a slowly releasable pool (SRP; also about 3 SVs per active zone) with a time constant about five to ten times larger (Sakaba and Neher, 2001; Ritzau-Jost et al., 2014). Mostly the FRP contributes to EPSCs during a train of action potentials (APs; Sakaba, 2006). Nevertheless, a recent study suggests that the SRP can be converted to FRP after FRP depletion and that it does contribute to the steady-state response during prolonged AP trains (Lee et al., 2012). This raises the possibility that SRP and FRP represent two consecutive stages of maturation along the path of vesicles toward exocytosis.

Variance analysis of peak postsynaptic current amplitudes suggests a binomial model of synaptic release where the binomial constant N represents the number of release units (Clements, 2003). The interpretation of release units has varied, but recent evidence suggests that they are vesicular docking sites (alternatively called release sites), with one to several docking sites per active zone (Silver et al., 2003; Ruiz et al., 2011; Trigo et al., 2012; Pulido et al., 2015). However, accurate determinations of N and of the RRP size are difficult, particularly at large, multisite synapses (Taschenberger et al., 2005), making the relation between N and RRP size uncertain. Yet determining this relation is essential to develop a quantitative picture of synaptic function.

To measure the RRP size, we propose here a new approach based on the examination of the statistics of released SV numbers at single active zones. At individual synapses between cerebellar parallel fiber (PF) and molecular layer interneuron (MLI), multivesicular release is observed, suggesting the presence of several docking sites per active zone (Crowley et al., 2007; Bender et al., 2009; Satake et al., 2012). These synapses, like other synapses of the mossy fiber-PF-Purkinje cell pathway, are adapted to respond to bursts of activity at high frequency,

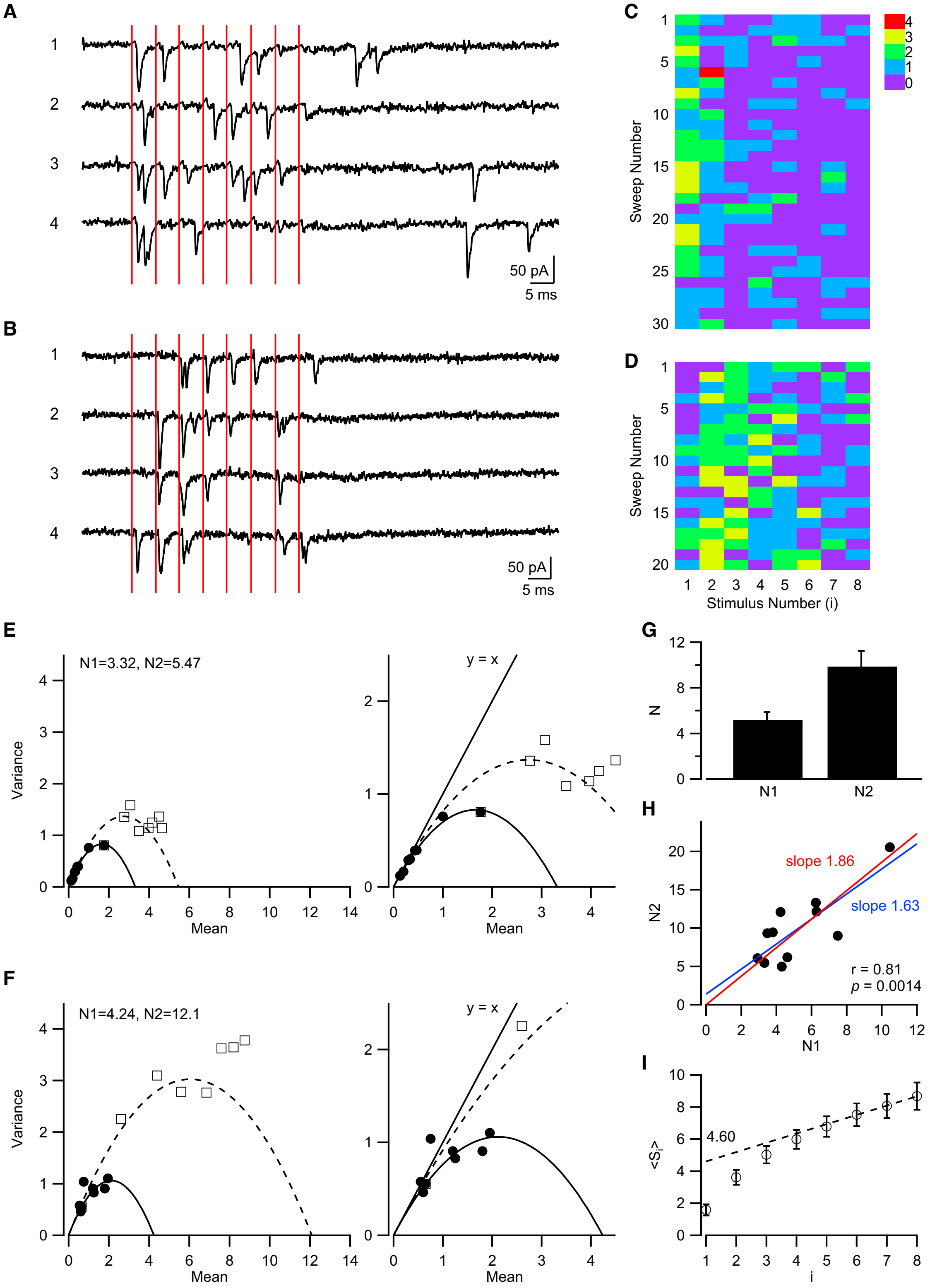

Figure 1. Variances of Phasic and of Cumulative Counts of Released Vesicle Numbers at Simple Synapses

(A and B) Representative recordings showing individual EPSCs elicited by trains of extracellular stimulations (vertical lines; 200 Hz; inter-train intervals, 10 s) in two different single PF-MLI connections. Criteria to select single connections were as described (“simple synapses,” Malagon et al., 2016).

(legend continued on next page)

putting high demands on RRP replenishment (Chadderton et al., 2004; Saviane and Silver, 2006; Valera et al., 2012; Ritzau-Jost et al., 2014). Quantal size is very large, so that released SVs can be counted using a matched-filter approach, based on deconvolution (Malagon et al., 2016). Using SV counts, we perform an investigation of release fluctuations that is more thorough than in studies using traditional approaches. In particular, we extract information on the organization of the RRP and on its mechanisms of replenishment from a fluctuation analysis of cumulative SV release evoked by an AP train. Our results suggest two sequential vesicular pools analogous to the SRP and FRP: a replacement vesicle pool and a docked vesicle pool. They further indicate that during an AP train the transfer from the replacement pool to the docked pool has a very rapid rate constant, much faster than previously estimated vesicular replenishment rates. Finally, our results indicate that the replacement step can be specifically inhibited by latrunculin B or blebbistatin, suggesting the involvement of actin and myosin II.

RESULTS

Variance Analysis of Cumulative versus Phasic Numbers of Released SVs

In the present work, we used recordings from PF-MLI synapses comprising a single presynaptic active zone and a single postsynaptic density (“simple synapses”) to count individual release events (Malagon et al., 2016). Using sagittal slices, we carefully positioned a θ-glass stimulation pipette at the slice surface to stimulate a candidate simple synapse, applying trains of 8 APs. Off-line analysis was used to distinguish simple and multiple synapses based on quantal amplitude CV and the extent of amplitude occlusion. Simple synapses have homogeneous quantal EPSC amplitudes. They display peak amplitude occlusion for consecutive EPSCs occurring at short time intervals (<5 ms), as these events activate a common set of postsynaptic receptors. In simple synapses, counts of evoked SVs following each AP were obtained by deconvolution, using mean quantal EPSCs as template (Malagon et al., 2016). In order to separate release of the RRP from later SV recruitment, we increased the release probability by raising the external Ca^{2+} concentration to 3 mM, and we stimulated at high frequency (200 Hz).

Figures 1A and 1B illustrate two representative experiments. SV counts s_i (color coded) are shown in Figures 1C and 1D, as a function both of stimulus number (i, columns) and of sweep number (lines). We modeled s_i statistics assuming several docking sites operating in parallel (Malagon et al., 2016). Calling N_1 the number of docking sites, and P_i the release probability at one docking site for stimulus number i, the mean and variance of s_i follow the relations

$$\langle s_i \rangle = N_1 \, P_i$$

$$\mathrm{var}\,(s_i) = N_1 \, P_i \, (1 - P_i),$$

such that

$$\mathrm{var}\,(s_i) = \langle s_i \rangle \, (1 - \langle s_i \rangle / N_1).$$

Note that in the above equation, in contrast to the classical analysis of EPSC amplitudes, the quantal size does not appear. N_1 is the only free parameter, and the initial slope of the var (s_i) plot as a function of $<s_i>$ is 1 (Figures 1E and 1F, right). The parabolic fits yield N_1 values of 3.32 and 4.24 for the two experiments shown (filled circles and continuous curves in Figures 1E and 1F). After determining N_1, P_i can be calculated as $P_i = <s_i> / N_1$. As discussed below, P_i is the product of the occupancy probability of one docking site by a SV with the probability that an occupied docking site releases its SV.

While the plots of var (s_i) as a function of $<s_i>$ provide estimates of N_1 and P_i, they give little information on the replenishment of empty docking sites. To approach this issue, we examined the sum S_i of successively released SVs, defined as $S_i = s_1 + s_2 + \ldots + s_i$. Without replenishment, the sum of released SVs is constrained by the number of SVs that were release ready before stimulation, and values for var (S_i) plotted as a function of $<S_i>$ should lie on the var (s_i) parabola (see below). As will become apparent, various replenishment models lead to different modes of interaction between successive s_k values and consequently to deviations from this simple expectation.

As shown in Figures 1E and 1F (open symbols), the data representing the dependence of var (S_i) on $<S_i>$ lie outside the “N_1 parabola” describing the relation of var (s_i) on $<s_i>$. They can, however, be fitted by another parabola (“N_2 parabola”), also with an initial slope of 1 (Figures 1E and 1F, dashed curves), and characterized by a new maximum value N_2, with $N_2 > N_1$ (N_2 = 5.47 in Figure 1E, and 12.1 in Figure 1F). Nevertheless, the shape of the var (S_i) versus $<S_i>$ curve varies significantly among experiments. While Figure 1E shows an example of a parabolic fit extending up to i = 8, in many experiments the data points gradually depart from the N_2 parabola for i values larger than 4, approaching an ascending line (Figure 1F). Meanwhile, the first point of the var (S_i) curve is located on the N_1 parabola, since $S_1 = s_1$, giving var (S_1) = var (s_1), and therefore this point is always inside the N_2 parabola. In view of these limitations, the fit of var (S_i) with the N_2 parabola was performed on a restricted dataset with i values of 2–4, while the fit of var (s_i) used

(C and D) Deconvolution analysis of the same traces yielded counts of released synaptic vesicles (from 0 to 4; each column corresponds to a stimulus number i, and each sweep to a train; sweep numbers match in A–C and B–D).

(E and F) Having calculated the mean and variance of released vesicle numbers, $<s_i>$ and var (s_i), var (s_i) is plotted as a function of $<s_i>$ for the two experiments shown in (A) and (B) (filled circles). These plots can be approximated by parabolas with maximum values N_1 = 3.32 (E) and N_1 = 4.24 (F). Also the cumulative number of vesicles $S_i = s_1 + s_2 + \ldots + s_i$ is calculated, and var (S_i) is plotted as a function of $<S_i>$ (open symbols). These plots can be approximated by other parabolas with maximum values N_2 = 5.47 (E) and N_2 = 12.1 (F). (Right panels) Expanded plots near origin, with y = x reference line. Using the relation $<s_i> = N_1 P_i$ and the above values of N_1, the maximum of P_i occurs for i = 1 in (E) (P_1 = 0.53) and for i = 2 in (F) (P_2 = 0.46).

(G) Average values of N_1 and N_2 across experiments (m. ± SEM, n = 11).

(H) Plotting N_2 as a function of N_1 reveals a significant correlation (blue, regression line; p = 0.0014). Fitting line passing through the origin (red) has a slope of 1.86.

(I) Average $<S_i>$ data (m. ± SEM, n = 11). Back extrapolation of a linear fit of the late part of the $<S_i>$ curve to i = 1 yields an RRP estimate of 4.60.

the entire range of i values (1–8). Average values obtained in this manner are $N_1 = 5.20 \pm 0.68$ and $N_2 = 9.87 \pm 1.38$ ($n = 11$; Figure 1G; ratio between the two averages, 1.9). Examination of individual experiments reveals marked variations in both N_1 values and N_2 values (Figures 1E and 1F). When N_2 is plotted as a function of N_1, a highly significant correlation is found ($p = 0.0014$; Figure 1H; blue, regression line). When fitting the N_2 versus N_1 relationship with a line passing through the origin, we found a slope of 1.86, close to 2 (red, Figure 1H).

Group $<S_i>$ results from 11 experiments are displayed in Figure 1I. Due to synaptic depression, $<S_i>$ increments decrease near the end of the train. To obtain an estimate of the RRP size, we performed a back extrapolation of the late linear part of the $<S_i>$ versus i curve (Schneggenburger et al., 1999), yielding a value of 4.60 per synapse (Figure 1I). This estimate of the RRP size is close to that of N_1 (5.2 in Figure 1G); however, it will be argued below that this similarity is partially accidental.

In summary, while var (s_i) versus $<s_i>$ data follow a parabola, as expected from a binomial model, var (S_i) versus $<S_i>$ data cannot be described with the same parabola. Rather, they can partially be approximated with another parabola having a maximum vesicle number about twice the value found for the first parabola, or in other words, twice the docking site number. Below we investigate which release models display such statistical properties.

Simulations of Var (S_i) versus $<S_i>$ Curve in Various Release Models

To obtain insight into cellular mechanisms that could account for the results of Figure 1, we next performed Monte Carlo simulations of several plausible models of simple synapses. We assume four independent and equivalent docking sites ($N_1 = 4$). At each docking site the probability of release for stimulus i is the product of docking site occupancy, δ_i, and of the probability of docked SVs to release, p: $P_i = \delta_i\, p$. We assume here that p is the same for all stimuli. Below, we will examine the possibility that p changes during the train. We note $\delta_1 = \delta$ for the docking site occupancy at rest, before the first stimulus. The plots in Figures 2A–2E assume the arbitrary values $\delta = 0.8$ and $p = 0.6$. All models predict binomial or nearly binomial distributions with maximal value $N_1 = 4$ for s_i, so that var (s_i) points are on the N_1 parabola or close to this parabola. The models differ, however, in the shape of the var (S_i) versus $<S_i>$ curve.

We first consider a simple docking site model where docked SVs are not replaced after release. In this case, S_i, like s_i, follows binomial statistics with $N_1 = 4$, so that the var (S_i) versus $<S_i>$ curve coincides with the var (s_i) versus $<s_i>$ curve, with the only difference being that the range covered by the var (S_i) points extends to larger abscissa values (Figure 2A). Values on the S_i parabola would approach the baseline, had we chosen a value for δ near 1. This model does not account for the departure of experimental var (S_i) values from the N_1 parabola as soon as i is larger than 1.

We next consider a variant of the previous model where following exocytosis of docked SVs, release continues according to a Poisson process (one-step + Poisson model). This model assumes a parallel pathway of vesicular release implicating an initially empty pool of SVs. After the first stimulation, this vesicular pool starts being replenished following a Poisson process with a probability of f per interspike interval. When SVs are present in the pool, they release with a probability of p_2. In this case, the var (S_i) versus $<S_i>$ curve soon exceeds the values of the N_1 parabola and approaches a linear relationship with a slope close to 1 (Figure 2B). This model captures some of the features of the data, but it displays an early transition to an asymptotic line that differs from actual var (S_i) curves.

We then consider a second variant where SVs reoccupy the site with a transition probability s (calculated for one interstimulus interval) if the site has become empty (renewable one-step docking site model). This produces an upward trend in the var (S_i) curve, similar to that of Figure 2B but with a lower limiting slope (Figure 2C).

In a further variant, empty docking sites are replenished by associated sites called replacement sites (two-step model without replenishment: Figure 2D). Whereas the initial occupancy of docking sites, δ, is free to take values <1, in conformity with previous work (Trigo et al., 2012; Pulido et al., 2015), we assume for simplicity that the initial occupancy of the replacement site, ρ, is fixed at 1 and that the number of replacement sites is equal to that of docking sites. The transition from an occupied replacement site to an emptied docking site during an interstimulus interval has a probability r. In this model, S_i does not strictly obey a binomial distribution for each i value, except for $i = 1$ where $S_1 = s_1$. However, values of S_i cannot exceed the total number of docking sites and replacement sites, which is $2N_1$. After several stimuli, the release probability of individual SVs does not depend much on whether the SV was initially located on a docking site or on a replacement site, and the S_i distribution approaches a binomial with maximum $N_2 = 2N_1$. Accordingly, the simulated var (S_i) curve can be fitted with a second parabola giving $N_2 = 7.84$, close to $2N_1$ (dotted line, Figure 2D). Overall, this model is a good representation of some experiments such as that of Figure 1E, and it provides the rationale for fitting var (S_i) data with a wider N_2 parabola.

The final variant adds a replenishment step, with probability s, to the replacement SV pool once sites in this pool are vacated (renewable two-step model, Figure 2E). In this model the var (S_i) curve displays a sequence of downward and upward curvatures. The deviation of S_i statistics from a binomial is now severe. Not only do the first points deviate because of the mix between docked and replacement SVs, as in the previous model, but in addition, near the end of the train, the participation of new SVs provided by the replenishment step induces a new escape from the N_2 parabola. The overall shape of the var (S_i) curve is close to that found in a majority of the experiments, as illustrated in Figure 1F. In spite of the deviations from the N_2 parabola for low and large i values, points for $i = 2$–4 are reasonably close to the N_2 parabola, and fitting these points with a parabola with free N value gives $N_2 = 8.84$, close to the theoretical value of 8.

Of the models just considered, only three (B, C, and E) at least grossly mimic experimental data. To help distinguish between these models, we next performed least-squares fits of the var (S_i) versus $<S_i>$ curve. To reduce errors linked with N_1 variations, data were averaged from a subset of six experiments with

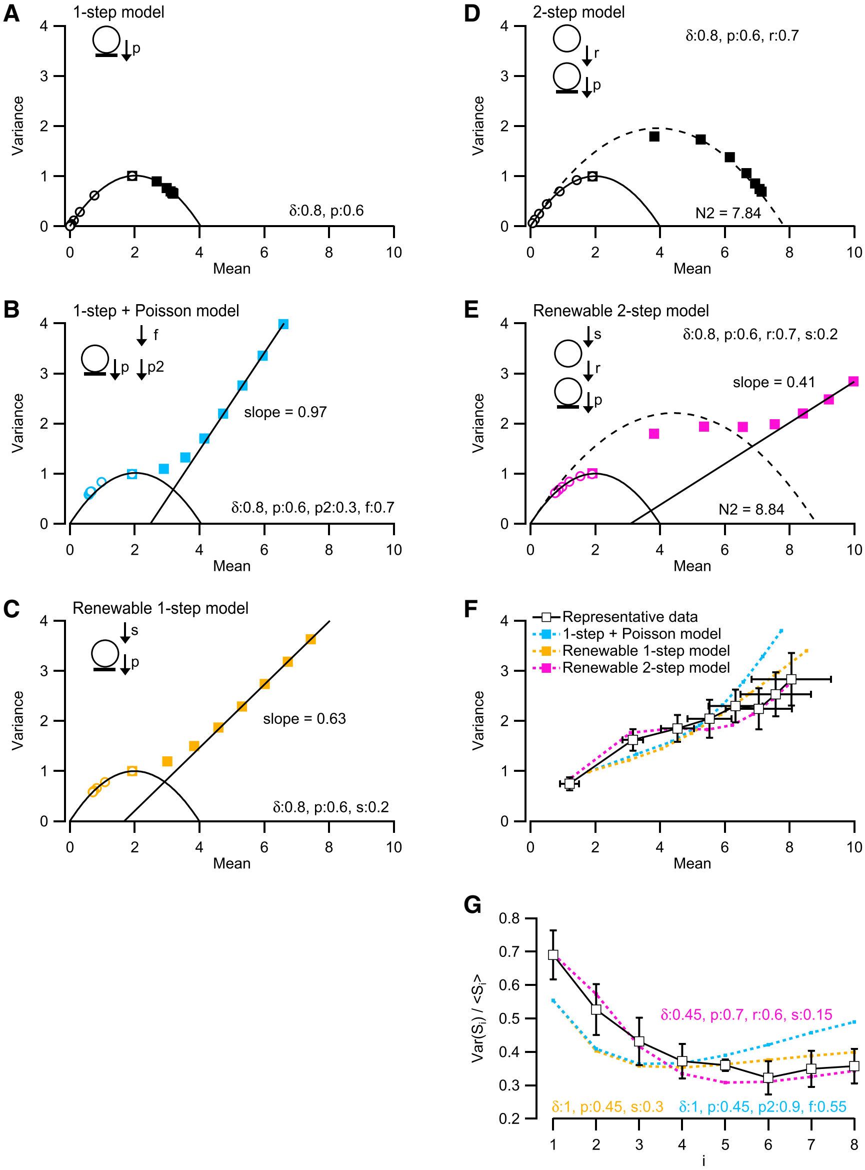

Figure 2. Statistics of Cumulative Released Vesicle Numbers in Various Docking Site Models

A series of Monte Carlo simulations of var (s_i) versus $<s_i>$ plots (circles) and of var (S_i) versus $<S_i>$ plots (squares) were performed using various synapse models with four docking sites. Synapses are subjected to trains of 8 APs at 200 Hz as in Figure 1. In (A)–(E), the model assumes an initial docking site occupancy δ = 0.8 and an occupied docking site release probability p = 0.6, independent of i.

(A) In the simplest variant, released vesicles are not replaced (one-step model without replacement). In this case, both var (s_i) (circles) and var (S_i) data (squares) fall on the N_1 parabola; closed symbols merely extend the range of this parabola that is explored.

(B) In this model, release continues after the exhaustion of docked vesicles as a Poisson process, either through the docking sites or elsewhere in the synapse (one-step model + Poisson). In this case, the var (S_i) points depart from the N_1 parabola to approach a line with a slope close to 1.

(C) In the renewable one-step model, emptied docking sites are replenished from an infinite vesicle pool with a fixed transition probability s.

(D) Here four replacement sites are paired to four docking sites (two-step model without replacement). Each replacement site supplies vesicles once the corresponding docking site is empty, with a probabilility r = 0.7. Once empty, replacement sites are not replenished. var (S_i) points form a second parabola with extrapolated value N_2 = 7.84.

(E) Same as in (D), but now the replacement sites, once emptied, can be replenished with a rate constant s (renewable two-step model). var (S_i) points depart from the N_2 parabola for $i \geq 4$, approaching a line with a slope of 0.41. A parabolic fit of var(S_i) versus $<S_i>$ plot restricted to i = 2–4, as performed in Figure 1, yields N_2 = 8.84, similar to the exact value N_2 = 8.

(F) Least-squares fits of var (S_i) versus $<S_i>$ data. To minimize intersynaptic heterogeneity experimental points are taken from the group of 6 cells in Figure 1H with N_1 values comprised between 2.5 and 4.5. After averaging, the data were scaled to N_1 = 4 for comparison with simulations (black squares; error bars, ±SEM). Summed squared deviations are much smaller for the sequential model with replacement site (0.35, with best fit values δ, 0.45; p, 0.7; r, 0.6; and s, 0.15; red) than for the one-step + Poisson model (3.23, with best fit values δ: 1, p: 0.45, p_2: 0.9, f: 0.55; blue) or for the renewable one-step model (3.35, with best fit values δ, 1; p, 0.45; s, 0.3; yellow).

(G) Plot of var (S_i) / $<S_i>$ versus i. Simulated results are from the same three models as in (F). The renewable two-step model best approximates the data.

estimated N_1 values comprised between 2.5 and 4.5 and were scaled to N_1 = 4, making them directly comparable to the N_1 = 4 simulations. Model E provides the best approximation to the data (Figure 2F, red curve). The best parameter combination for model E indicates that at rest, almost half of the docking sites are occupied (δ = 0.45), that the probability of an occupied site to release is elevated (p = 0.7, so that $P_1 = 0.45 \times 0.7 = 0.315$, similar to the value of 0.38 estimated at 2 mM Ca_o at PF-MLI synapses by Ishiyama et al., 2014, and to the value of 0.31 estimated at 2.5 mM Ca_o at PF-Purkinje cell synapses by Valera et al., 2012). The best fit also suggests that the probability of transition from filled replacement site to empty docking site (r = 0.6) is larger than that to refill an empty replacement site (s = 0.15). This leads to gradual depletion of both docking sites and replacement sites near the end of a stimulation train.

Experimental results (right panels in Figures 1E and 1F) show that near steady state, the ratio var (s_i)/ $<s_i>$ is close to 1. By contrast, the var (S_i)/ $<S_i>$ ratio is markedly smaller than 1 for all values of i. It declines gradually for increasing i, and it assumes a value close to 0.35 for i > 4 (Figure 2G). While model E (red curve) correctly reproduces the shape of the var (S_i)/ $<S_i>$ curve, both model B and model C deviate from the data, starting with too low a value at i = 1 and reaching a minimum at i = 3 before rising again for larger i values (blue and orange curves,

Figure 2G). This analysis confirms that model E is a better representation of the data.

Overall our simulations favor a renewable two-step docking model, more simply called ''two-step model'' thereafter, where SVs transit through a replacement site and a docking site before being released.

Accuracy of N_1 and N_2 Estimates

The stochastic nature of synaptic transmission generates some degree of uncertainty on the values of N_1 and N_2 that are derived from a given experiment. To estimate this uncertainty, we performed a series of simulations of individual experiments containing 30 trials each, using the two-step model with $N_1 = 4$, $N_2 = 8$, and the optimal parameter values illustrated in Figures 2F and 2G. These simulations gave $N_1 = 4.11 \pm 1.12$ and $N_2 = 8.19 \pm 1.50$ (m ± SD; see Figures S1A–S1C available online). These results lead to CV values of 0.27 for N_1 and 0.18 for N_2 in simulated experiments, versus 0.43 and 0.46 as calculated from the results of Figure 1G, indicating that only part of the variability observed among individual N_1 and N_2 values originates from stochastic uncertainty. We interpret the additional variance as reflecting genuine variations among simple synapses. Consistent with this view, the correlation between experimental N_1 and N_2 values (Figure 1H) had a larger Pearson's coefficient (0.81) and larger regression line slope (1.63) than the corresponding correlation in simulated data (0.41 and 0.55, respectively; Figure S1D). These results indicate concerted variations of N_1 and N_2 among simple synapses.

Because the fit of the N_2 parabola only applies in a restricted range of stimulation numbers, we next asked how accurate is the value of N_2 derived from this fit, even if an infinite number of trials could be obtained. To this end, within the framework of the two-step model, we performed additional simulations, varying individually each parameter around its optimum value while keeping the other three parameters constant, and we evaluated the resulting changes in estimated N_2 values. This gave values similar to the target value of 8 ($7 \leq N_2 \leq 9$) for large ranges of each of the four parameters ($0.3 \leq \delta \leq 1$; $0.3 \leq p \leq 1$; $0.2 \leq r \leq 1$; $0 \leq s \leq 0.3$; Figure S2). Therefore the parabolic fit to var (S_i) data gives approximately correct values of N_2 for large parameter ranges.

Measurement of Presynaptic Calcium Increments

Our simulations show that the two-step model accounts for $<s_i>$ and var (S_i) curves without necessitating any change of p with i. In other preparations, such as the calyx of Held, however, Ca^{2+} entry facilitates during AP trains, thus increasing p (Hori and Takahashi, 2009). To explore this possibility, we loaded granule cells with the Ca^{2+} indicator Oregon Green BAPTA-6F (OGB-6F, 500 μM), and we performed two-photon imaging experiments of single axonal varicosities during AP trains at 200 Hz (Figure 3). Peak amplitude ratios between fluorescence signals for 1 and 2 APs were on average 1.85 ± 0.05 (n = 9; six varicosities from ascending axons, and three varicosities from PFs; results did not differ between the two groups and were therefore pooled together). Group results (n = 8) for one to 8 APs displayed a slightly sublinear dependence on AP number (Figure 3D), reflecting gradual saturation of OGB-6F (blue curve). After correcting for dye saturation, a linear relation between Ca^{2+} concentration increments and AP number was found, with a slope of 0.21 μM/AP (Figure 3E). These results indicate, in agreement with a previous report (Brenowitz and Regehr, 2007), that the amount of presynaptic Ca^{2+} entry in single PF varicosities does not vary during AP trains.

The results of Figure 3 indicate little decrement of Ca^{2+} signals between individual APs and therefore a substantial accumulation of residual Ca^{2+} during trains. From the increase in volume-averaged Ca^{2+} rise of 0.21 μM/AP in the presence of OGB-6F, and a previous estimate of the intrinsic buffering capacity of PF terminals (56; Brenowitz and Regehr, 2007), a corrected value of 0.58 μM/AP of volume-averaged Ca^{2+} rise is obtained in intact varicosities (see Supplemental Information). Thus, while the volume-averaged data of Figure 3E do not indicate an increase of Ca^{2+} entry during the train, the possibility remains that Ca^{2+} elevation could induce an increase in local Ca^{2+} concentration rises following saturation of endogenous buffers (Eggermann et al., 2011).

One-Step Models with Varying p Values

Since standard models of facilitation assume that p increases after the first stimulus, we next asked whether a modified version of one of the one-step models of Figure 2 could account for the results when incorporating changes in p. First we note that neither variant of the one-step model (one-step model + Poisson, and renewable one-step model) can account for the $<s_i>$ curve if p is constant. Thus the optimum parameter sets corresponding to the best fits of the var (S_i) curve display depression instead of facilitation (Figure S3A). To correct this situation, we introduced a 2-fold increase of p from the second stimulus until the end of the train ($p_i/p_1 = 2$ for i = 2–8). After re-optimization of the parameter sets, $<s_i>$ curves now approached experimental data (Figure S3B), but neither the var (S_i) nor the var (S_i) / $<S_i>$ curve could be fitted well (Figures S3C and S3D). These results indicate that even after ad hoc adjustment of p during a train, one-step models remain inferior to the two-step model.

Analysis of Covariance

The low var (S_i) values apparent in experiments and in simulations (Figure 2G) are very striking. They show that late vesicle recruitment does not follow the predictions of a random process with low success rate, because in that case the ratio var (S_i) / $<S_i>$ would be close to 1. To explain the low value that is experimentally observed for this ratio (near 0.35), it seems necessary to envisage a compensatory mechanism such that in a trial where the sum of responses S_i is particularly large for index i, the subsequent release s_{i+1} tends to be lower than its average $<s_{i+1}>$. This predicts a negative covariance between S_i and s_{i+1}, since by definition covar (S_i, s_{i+1}) = $<S_i - <S_i>> <s_{i+1} - <s_{i+1}>>$. On a mechanistic level, docking site occupancy creates a negative correlation between the release probability of a given stimulus and that of the subsequent one (Scheuss and Neher, 2001), in agreement with experimental findings at the calyx of Held (Scheuss et al., 2002). This negative correlation is likely more pronounced for two sites in series (as in model E above) than for a single docking site. In order to test these predictions, we studied the amount of covariance observable among successive s_i values, as well as between S_i and s_{i+1}.

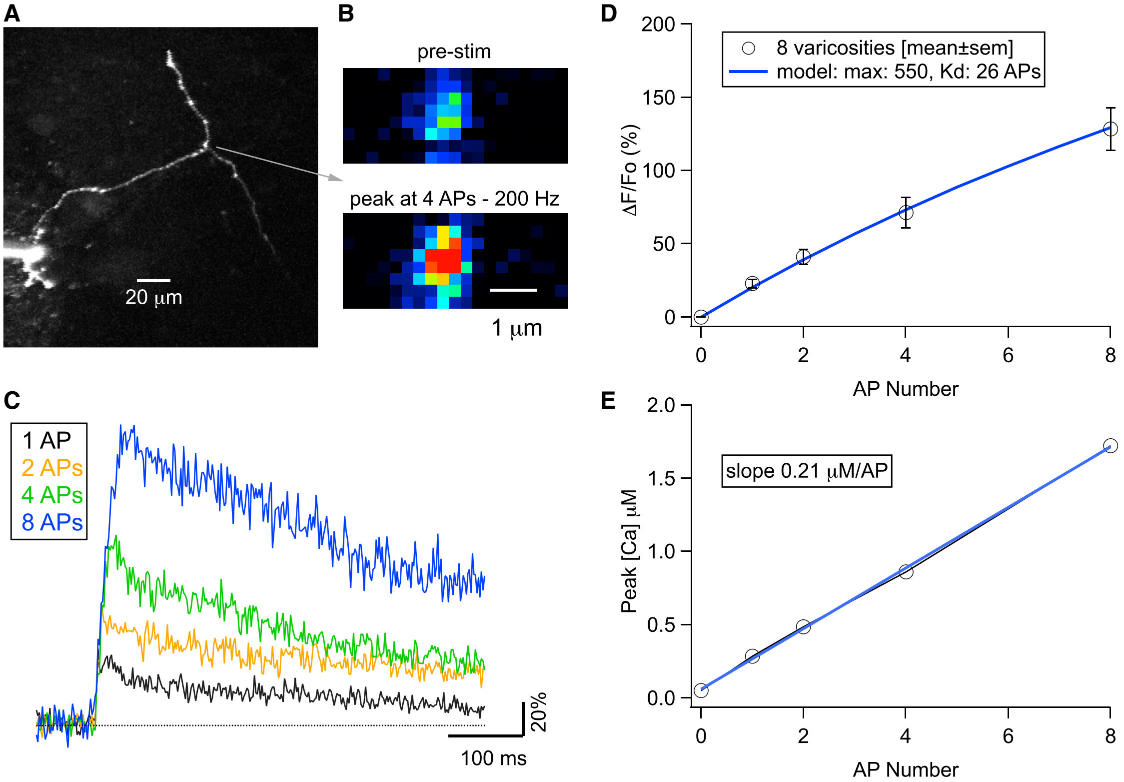

Figure 3. Linear Dependence of Presynaptic Calcium Entry on AP Number in Single Granule Cell Varicosities

(A) Maximum intensity projection from two-photon laser scanning of Alexa 594 fluorescence in a granule cell.

(B) Two-photon scans of a selected varicosity in the same granule cell. The image was taken with the green channel and corresponds to OGB-6F fluorescence.

(C) Time course of $\Delta F/F_o$ for 1, 2, 4, and 8 AP trains at 200 Hz, from the varicosity displayed in (B).

(D) AP-evoked peak $\Delta F/F_o$ values (open circles, m. ± SEM, n = 8 varicosities) are fitted with a hyperbolic function (blue) derived from the sensitivity of OGB-6F on Ca^{2+} concentration (see SI), where half saturation occurs for 26 APs.

(E) Replotting the data in (D) using OGB-6F calibration (see Supplemental Information), assuming a low basal Ca^{2+} concentration (50 nM), indicates a linear dependence of Ca^{2+} entry on AP number (blue).

By virtue of covariance bilinearity,

$$\mathrm{covar}\,(S_i, s_{i+1}) = \mathrm{covar}\,(s_i, s_{i+1}) + \mathrm{covar}\,(s_{i\text{-}1}, s_{i+1}) + \mathrm{covar}\,(s_{i\text{-}2}, s_{i+1}) + \ldots + \mathrm{covar}\,(s_1, s_{i+1}).$$

As a rule, covariance values are largest for consecutive stimulations, so that the largest contribution in this sum likely arises from the first term, covar (s_i, s_{i+1}). Experimental values of covar (s_i, s_{i+1}) were calculated for the 11 experiments of Figure 1, and the results are plotted as a function of i in Figure 4A. Their means are negative, starting from about −0.2 for i = 1 or 2 and decreasing in size thereafter. However, data display scatter, and the covariance is significantly negative only for i = 1–3 ($p < 0.05$ in each case).

The corresponding plot for covar (S_i, s_{i+1}) is shown in Figure 4B. As expected, the plot displays again negative values, starting with the same value near −0.2 for i = 1, but now the size of the covariance grows for i = 2 and 3, before decreasing again at larger i values. Overall the covariance is significantly negative for all i values except for i = 6 ($p < 0.05$). The average covar (S_i, s_{i+1}) value is about −0.15 for i = 6 and 7.

If N_1 independent and equivalent docking sites operate in parallel, covariance bilinearity implies that

$$\mathrm{covar}\,(S_i, s_{i+1}) = N_1\,\mathrm{covar}\,(X_i, x_{i+1}),$$

where X_i and x_{i+1} represent cumulative and phasic numbers of SVs released at one docking site (Scheuss and Neher, 2001). Therefore, under the above assumption, covar (S_i, s_{i+1}) should be proportional to N_1. This prediction is examined in Figure 4C, where it can be seen that covar (S_i, s_{i+1}) is correlated to N_1 ($p < 0.01$; blue regression line) and that the relation between the two parameters is close to proportionality (red). This indicates that docking sites are equivalent and operate independently of each other.

We finally compared simulation results for models B, C, and E of Figure 2 (with $N_1 = 4$) to experimental data (Figure 4D). While all three models predict negative covariance, model E alone could mimic the dependence of covariance on i (red curve).

In conclusion, there is a negative correlation between successive vesicle counts. This translates into a negative covariance for both (s_i, s_{i+1}) and (S_i, s_{i+1}) couples that is predicted by the

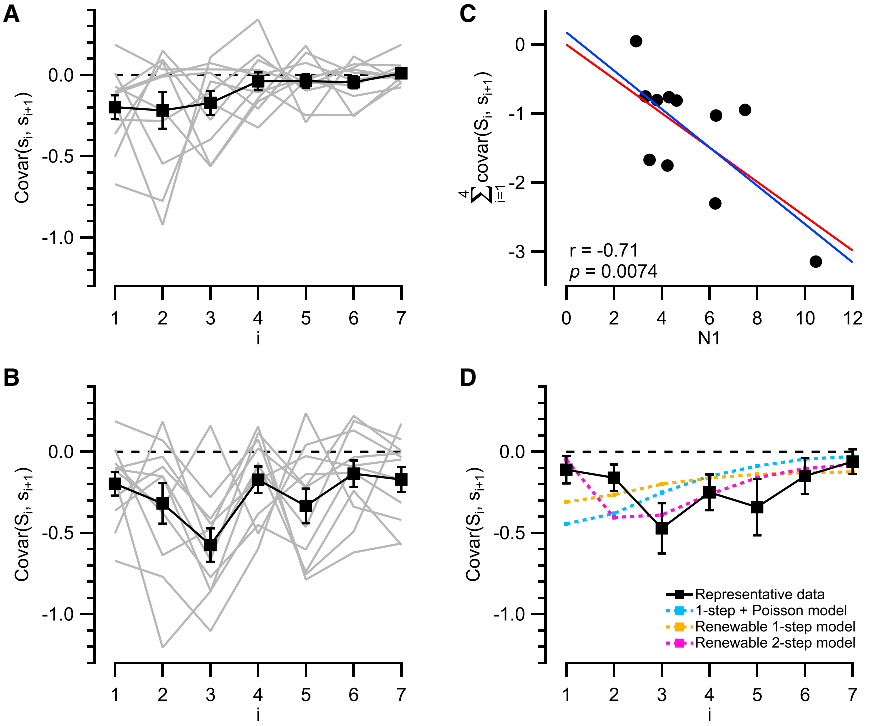

Figure 4. Covariance analysis of phasic and cumulative vesicle counts

(A) Covariance was calculated between consecutive counts (s_i, s_{i+1}). Results of individual experiments (gray lines; as before, 8 AP trains at 200 Hz) and group results (black; n = 11; m. ± SEM) as a function of i.

(B) Same as in (A), except that s_i is replaced by the cumulative count S_i. Covariance values are now larger.

(C) Plot of the sum of covar (S_i, s_{i+1}) for i = 1–4, as a function of N_1. The results show a significant correlation (p = 0.0074). The regression line (blue) is almost superimposed on the linear fit constrained to passing through the origin (red), indicating proportionality between covar (S_i, s_{i+1}) and N_1.

(D) Simulation of covariance. Monte Carlo simulations of the various models of Figures 2F and 2G were used to produce covariance results. Data have been restricted to the six cells with N_1 values ranging from 2.5 to 4.5, and scaled to N_1 = 4, as in Figures 2F and 2G. The renewable two-step model (red) offers the best approximation to the data.

two-step model and is consistent with the low variance of cumulative SV numbers near steady state.

Fast Recruitment of New Docked SVs from the Replacement Site

The simulations of Figure 2E indicate a value of 0.6 for r, the transition probability during an interstimulus interval Δt from a filled replacement site to an empty docking site. Assuming a rate constant R for this transition, we have r = 1 – exp (−R Δt). With Δt = 5 ms, we obtain R = 183 s^{-1}. This value is surprisingly large—so large that it exceeds the predictions based on unrestrained SV diffusion, as shown in the following.

The diffusion coefficient of a SV can be calculated according to Stoke's equation,

$$D = (k_B\ T)/(6\pi\ \eta\ a),$$

where k_B is Boltzmann's constant, T is temperature, η is viscosity, and a is the SV radius. Taking $\eta = 8.9 \times 10^{-4}$ Pa.s as the viscosity of water and a = 22.5 nm (Imig et al., 2014), we obtain D = 0.113 μm^2/s. Einstein's diffusion equation gives the mean displacement time of a diffusing SV over a distance 2a:

$$t = 4\ a^2/(2D) = 9.0\ \text{ms}.$$

Therefore, if a SV had to move by diffusion from the replacement site to the docking site by more than its diameter, the diffusion time would be longer than the interstimulus interval used here, which is 5 ms. It would also be longer than our estimate of the replacement time 1/R, which is 5.5 ms. These calculations suggest an active process in the transition from replacement site to docking site.

Pharmacological Manipulations

To further test the two-step model, we next tried to inhibit the replacement step—or in other words, to selectively reduce the transition probability r. Looking for possible blockers of this step, we were guided by the above calculation suggesting an active SV movement, possibly mediated by the cytoskeleton. We also noted a possible homology between docked SVs and replacement SVs on one side, and the FRP and SRP pools previously described in the calyx of Held on the other side (see Introduction). It was shown that the actin filament blocker latrunculin A inhibits FRP recovery after a train (Sakaba and Neher, 2003). It was further suggested that SRP SVs can refill the FRP during trains and that this process can be inhibited by the actin blocker latrunculin B or by the myosin II blocker blebbistatin (Lee et al., 2012). If replacement SVs of MLIs corresponds to the SRP of the calyx of Held, application of latrunculin B or blebbistatin should disrupt the refilling of docking sites from the replacement sites. To test this prediction, we next examined SV release statistics in the presence of these blockers. In addition, we also tried EGTA-AM treatment, because intracellular Ca^{2+} influences the renewal of vesicular pools (Hosoi et al., 2007; Neher and Sakaba, 2008).

The left column in Figures 5A and 5B illustrates an experiment in latrunculin B. Whereas control data often display facilitation (as in Figure 1B), in agreement with earlier studies (Atluri and Regehr, 1998; Bao et al., 2010; Ishiyama et al., 2014), responses in latrunculin B never exhibit facilitation (Figure 5A, left; Figure 5G, second panel). In latrunculin B, var (s_i) data are similar to control, building a parabola with N_1 = 2.39 in the example shown, but var (S_i) fails to form a distinct N_2 parabola. Rather, var (S_i) remains on the N_1 parabola up to i = 3, as illustrated by the squares labeled

1–3 in Figure 5B, left. For $i > 3$, var (S_i) rises almost linearly (Figure 5B, left), as in models of Figures 2B and 2C depicting one-step docking site situations. Average var (S_i) data from latrunculin B experiments are much closer together than in control, particularly for $i = 2–4$ (Figure 5C, left; $n = 9$; compare with Figure 5D).

Blebbistatin, like latrunculin B, abolishes facilitation (Figure 5A, middle column). However, late responses are less severely depressed in blebbistatin than in latrunculin B, and cumulative SV numbers are less reduced. In average var (S_i) data, an almost linear upward trend is observed for $i > 2$ (Figure 5C, middle panel).

Finally, incubation with EGTA-AM also inhibits facilitation, in agreement with earlier data (Atluri and Regehr, 1998; Figure 5A, right). In EGTA, both s_i and S_i responses are severely reduced for $i = 1–2$ compared to control (Figures 5B and 5C, right).

Group results did not reveal changes in the shape of the var (s_i) curve or in the value of N_1 associated to any of the three pharmacological manipulations (latrunculin B, $N_1 = 4.59 \pm 0.60$; blebbistatin, 4.28 ± 0.25; EGTA, 4.03 ± 0.71) with respect to control (5.20 ± 0.68; $p > 0.05$ in each case; Figure 5E). However, in all three pharmacological treatments, S_i values were below control values for $i > 1$, and RRP estimates obtained by back extrapolation of the S_i curve were markedly reduced (latrunculin B, 2.45; blebbistatin, 3.37; EGTA, 1.37; versus control, 4.60; Figure 5F). In addition, var (S_i) points remained much closer to the var (s_i) parabola for $i = 2–4$ after pharmacological treatment compared to control (compare red, blue, and green square locations in var [S_i] plots in models B and C with the corresponding control plot in model D). These results suggest that the pharmacological treatments do not modify the docking site number but that they do jeopardize the participation of replacement SVs to train responses, as expected from an inhibition of the replacement step (r).

Effects of Latrunculin B, Blebbistatin, and EGTA on $<s_i>$ Curve

While the above results are consistent with a disruption of the replacement step, additional or alternative effects on synaptic transmission remain possible. We compared quantal sizes in control conditions and after pharmacological treatments, finding no significant difference (control, 67.8 ± 9.2 pA; latrunculin B, 49.5 ± 7.0; blebbistatin, 57.1 ± 5.4 pA; EGTA-AM, 103.4 ± 14.4 pA; $p > 0.05$ in each case). This argues against postsynaptic effects. We next examined the values of s_1 following pharmacological manipulations. As shown in Figure 5G, $<s_1>$ values are not significantly altered in latrunculin B or blebbistatin (respectively, 1.28 ± 0.22 and 1.21 ± 0.17) compared to control (1.58 ± 0.35; $p > 0.05$ in each case). From the equation $<s_1> = N_1\ p\ \delta$ and the previous finding that N_1 is unchanged (Figure 5E), we conclude that the product $p\ \delta$ is not modified in both cases. The simplest interpretation is that neither p nor δ is modified. In EGTA by contrast, $<s_1>$ is significantly reduced (0.68 ± 0.11; $p < 0.05$), in agreement with previous results (Ishiyama et al., 2014). A likely interpretation is that EGTA decreases the amplitude and/or duration of the Ca^{2+} transient at the level of the Ca^{2+} sensor for exocytosis, leading to a reduction of p.

The rest of the $<s_i>$ curve reveals striking changes depending on the manipulation. In latrunculin B and in blebbistatin, facilitation is replaced by depression, with a steady-state value below control (Figure 5G, second and third panels; control values are superimposed in both cases). In EGTA, facilitation is also inhibited, but no depression is observed, and the steady-state value is similar to that of the control (Figure 5G, fourth panel). Paired-pulse ratios were calculated in each experiment as $<s_2> / <s_1>$. Group PPR results obtained in this manner display facilitation in control (PPR = 2.08 ± 0.47, $p < 0.05$), in agreement with earlier studies (Atluri and Regehr, 1998; Crowley et al., 2007; Bao et al., 2010; Satake et al., 2012; Ishiyama et al., 2014), but not in any of the three treatments (latrunculin B, 0.93 ± 0.45; blebbistatin, 1.13 ± 0.24; EGTA, 1.09 ± 0.14; $p > 0.05$ in each case; Figure 5H). The loss of facilitation may be explained, within the two-step model of Figure 2E, by a reduction of r (Lee et al., 2012). In control conditions, as r is large, replacement SVs are quickly recruited. They prevent a decrease in docking site occupancy early in the train, favoring facilitation. After r reduction, however, replacement SVs are recruited less efficiently. Their contribution is distributed more evenly among more stimuli, and depression predominates.

In conclusion, all three treatments aiming at reducing r result in an abolition of facilitation, suggesting a link between replacement SVs and facilitation.

Locus of Action of Latrunculin B, Blebbistatin, and EGTA

The above results indicate that r is the primary target of latrunculin B, blebbistatin, and EGTA. To test this notion more rigorously, we performed simulations of var (S_i) versus $<S_i>$ curves during pharmacological treatments. A least-squares analysis confirmed that latrunculin B and blebbistatin mainly altered r, while EGTA altered both r and p (Figure S4). Therefore we left r free to simulate latrunculin B and blebbistatin experiments, and both r and p free to simulate EGTA experiments, keeping other parameters at their control values (Figure 6A). The effects of latrunculin B and blebbistatin could be reproduced when reducing r by 6-fold and 2.4-fold, respectively. Simultaneous reduction of r and p (by 1.5-fold and 2-fold, respectively) mimicked the effects of EGTA. Using the relation $r = 1 - \exp(-R\ \Delta t)$, we obtain R values of 21 s^{-1} in latrunculin B, 58 s^{-1} in blebbistatin, and 102 s^{-1} in EGTA, with respective reductions relative to control by factors of 8.7, 3.2, and 1.8.

Reducing r led to a good fit for $<s_i>$ versus i curves (Figure 6A), as well as for var (s_i) versus $<s_i>$ curves (data not shown) but led to less satisfactory fits of var (S_i) versus $<S_i>$ curves, particularly in latrunculin B and in blebbistatin (Figure 6B). One possible reason for these discrepancies could be that latrunculin B and blebbistatin do not affect all docking sites to the same extent. A better fit was obtained by assuming that a fraction of docking sites (1/4 for latrunculin B, and 2/4 for blebbistatin) remains normally operating while the others are affected by the drug, either by severely reducing r (Figure S5) or by removing the replacement site altogether (Figure S6).

Another way to improve the fits of Figure 6B is shown in Figure 6C. In the calyx of Held, latrunculin, as well as various blockers of endocytosis, retards FRP recovery after prolonged stimulation, raising the possibility that under these conditions,

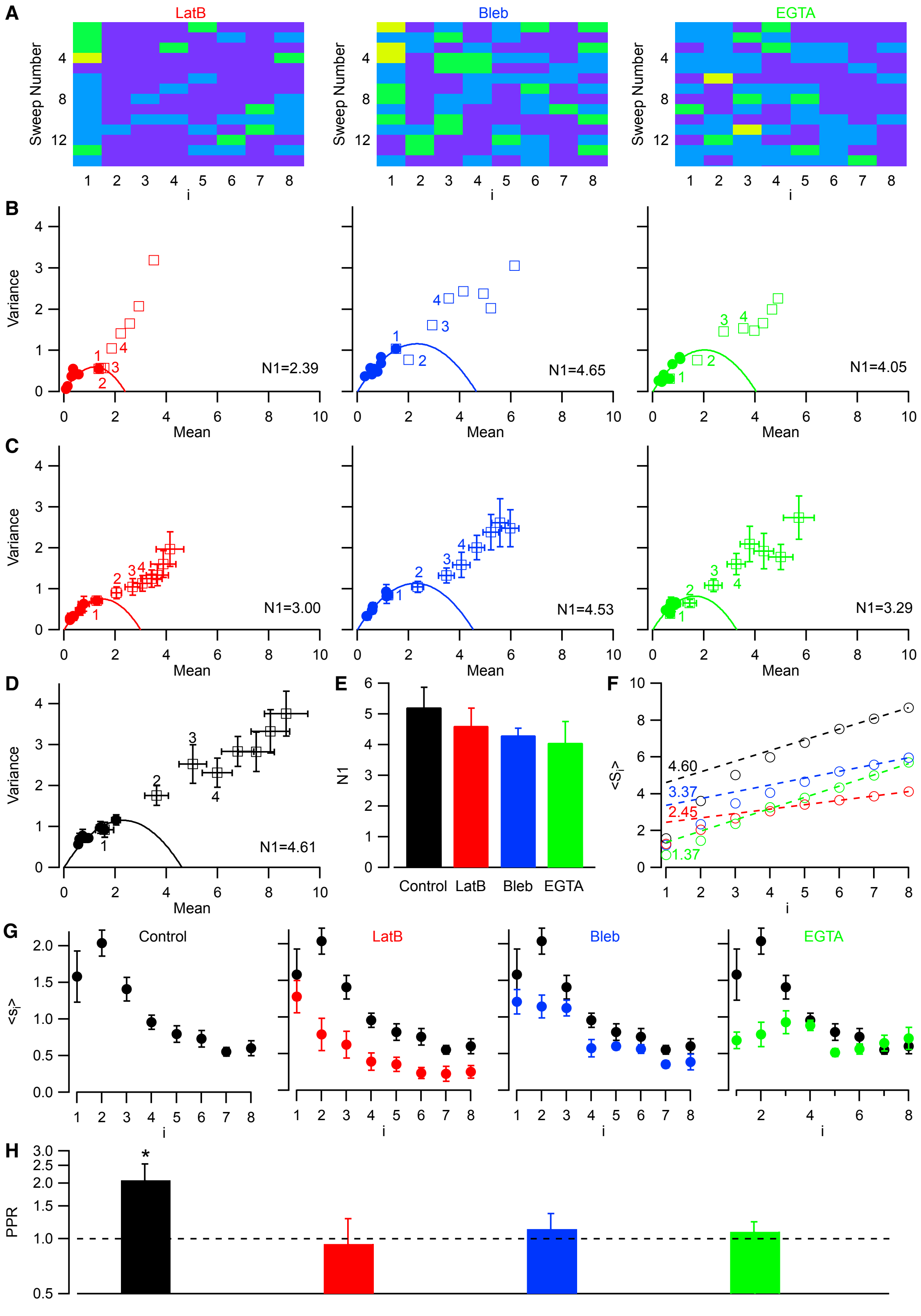

(legend on next page)

clearance of the docking site may be rate limiting (Sakaba and Neher, 2003; Hosoi et al., 2009; Neher, 2010). Therefore, we performed additional simulations of latrunculin B and blebbistatin data assuming a refractory period at individual docking sites of, respectively, 10 ms (Figure 6C, left) or 5 ms (Figure 6C, right) following exocytosis at that site, while neighboring sites were left free to release normally. This led to an improvement of the var (S_i) curve, while R values remained reduced compared to control (in latrunculin B, 32.5 s^{-1}; in blebbistatin, 71 s^{-1}; respective reduction ratios to control values, 5.6- and 2.6-fold). With the refractory period, s_i curves remained similar to those in experimental data (Figure 6D).

In summary, a reduction of r explains much of the effects of latrunculin B, blebbistatin, and EGTA both on $<s_i>$ and on var (S_i) curves. In addition, latrunculin B and blebbistatin may induce a refractory period following exocytosis, during which the docking site is unavailable for refilling, and EGTA results in a reduction of the exocytosis probability p. The reduction of r by latrunculin B and blebbistatin suggests that the translocation of replacement vesicles to the docking site involves actin and non-muscle myosin II.

Alternative Model with Two Types of Docking Sites

For the sake of simplicity, so far we have considered only models with equivalent docking sites. However, more complicated models incorporating heterogeneity among docking sites cannot be excluded. In particular, it is possible to account for the data of Figures 1 and 2 with two different types of single-step docking sites. However, the resulting model assumes a rather arbitrary sequential activation of two separate sets of docking sites during a train of stimuli (Figure S7). In addition, this model does not account easily for the effects of latrunculin B or of blebbistatin, and overall was not considered as an attractive alternative to the two-step model.

Extension of the Two-Step Model to Single GABAergic Synapses

Having shown that the two-step model applies to PF-MLI synapses, we next asked how general this scenario may be across synaptic types. Previous work has shown that some MLI-MLI synapses, called "elementary synapses," display a single docking site ($N_1 = 1$; Pulido et al., 2015; Figure 7A). Whereas extensive receptor saturation undermines SV counting at single GABAergic synapses containing several docking sites, no such effect occurs at elementary synapses. If elementary GABAergic synapses follow the two-step paradigm, their S_i data should display a parabola with N_2 close to 2. We next tested this prediction.

A representative experiment is illustrated in Figures 7B and 7C. As previously reported, elementary MLI-MLI synapses exhibit severe depression when repetitively stimulated at 25 Hz (Figure 7B). While var (s_i) follows a parabola with $N_1 = 1.0$, as expected, var (S_i) is well described by a wider parabola with $N_2 = 2.0$ (Figure 7C). Group results indicate $N_2 = 1.8 \pm 0.3$ (mean ± SEM, n = 7; Figure 7D), close to $N_2 = 2$. As a further test of the two-step model, we examined statistics of the sum of SV counts across the train, S_5. Average results (n = 7) show that the probability of observing S_5 values in the range from 0 to 2 is significant ($P(S_5 = 0) = 0.33 \pm 0.06$; $P(S_5 = 1) = 0.52 \pm 0.04$; $P(S_5 = 2) = 0.13 \pm 0.03$) but that $P(S_5 > 2)$ is very low (0.012 ± 0.008; Figure 7E). The data differ strikingly from a Poisson distribution with identical mean value (red curve in Figure 7E), and they suggest a strict restriction to have $P(S_5 \leq 2)$. The two-step model with $N_2 = 2$ provides precisely this restriction.

These results indicate that the two-step model applies to elementary MLI-MLI synapses. They therefore suggest that this model is not restricted to PF-MLI synapses, nor to glutamatergic synapses, and that it may be generally applicable.

DISCUSSION

The present work makes use of the newly developed method of counting vesicular release events at simple synapses (Malagon et al., 2016) to study the processes underlying docking site replenishment during trains. Using SV counting, we examined the stochastic properties of cumulative release numbers, S_i, obtained during a series of stimuli. We found that the variance of S_i is larger than that predicted by the simplest docking site model (one-step model without renewal). However, it is clearly smaller than the expectation for a renewal process that would be independent of previous release. Remarkably, var (S_i) values for i larger than 3–4 are very low and are accompanied by a negative covariance between S_i and the subsequent vesicle count s_{i+1}. These results are consistent with a model supposing two sites in sequence, a replacement site and a docking site. We furthermore found that the anti-actin drug latrunculin B, or the anti-myosin II drug blebbistatin, specifically inhibits the transition between replacement site and docking site. In both cases,

Figure 5. Effects of Latrunculin B, Blebbistatin, and EGTA on Release Statistics

(A) Representative experiments. Counts of released vesicles are examined after incubation with the actin anti-polymerization agent latrunculin B (15 μM, left column), with the anti-myosin II drug blebbistatin (100 μM, middle), and after treatment with EGTA-AM (10 min preincubation at 100 μM followed by wash, right).

(B) var (s_i) versus $<s_i>$ plots (filled circles) and var (S_i) versus $<S_i>$ plots (open squares; numbers indicate corresponding i values; note that the first square is always superimposed with a dot) for the experiments in (A).

(C) Summary plots from nine experiments in latrunculin B, seven in blebbistatin, and seven with EGTA.

(D) Summary plots from 11 experiments in control conditions.

(E) Group data showing no significant effects of latrunculin B, blebbistatin, or EGTA on N_1 values. Here parabolic fits were performed in individual experiments, whereas they were performed on group results in (C) and (D).

(F) Average $<S_i>$ plots, showing RRP estimates obtained by back extrapolation.

(G) Plots of $<s_i>$ versus i. In latrunculin B and in blebbistatin, s_1 is not significantly different from its control value; s_i decreases with i, and the steady-state value s_{ss} is significantly lower than in control. By contrast, after EGTA application s_1 is reduced, no depression is observed, and s_{ss} is similar to its control value.

(H) Whereas the paired-pulse ratio is larger than 1 under control conditions, indicating facilitation, it is not significantly different from 1 after any of the three pharmacological treatments.

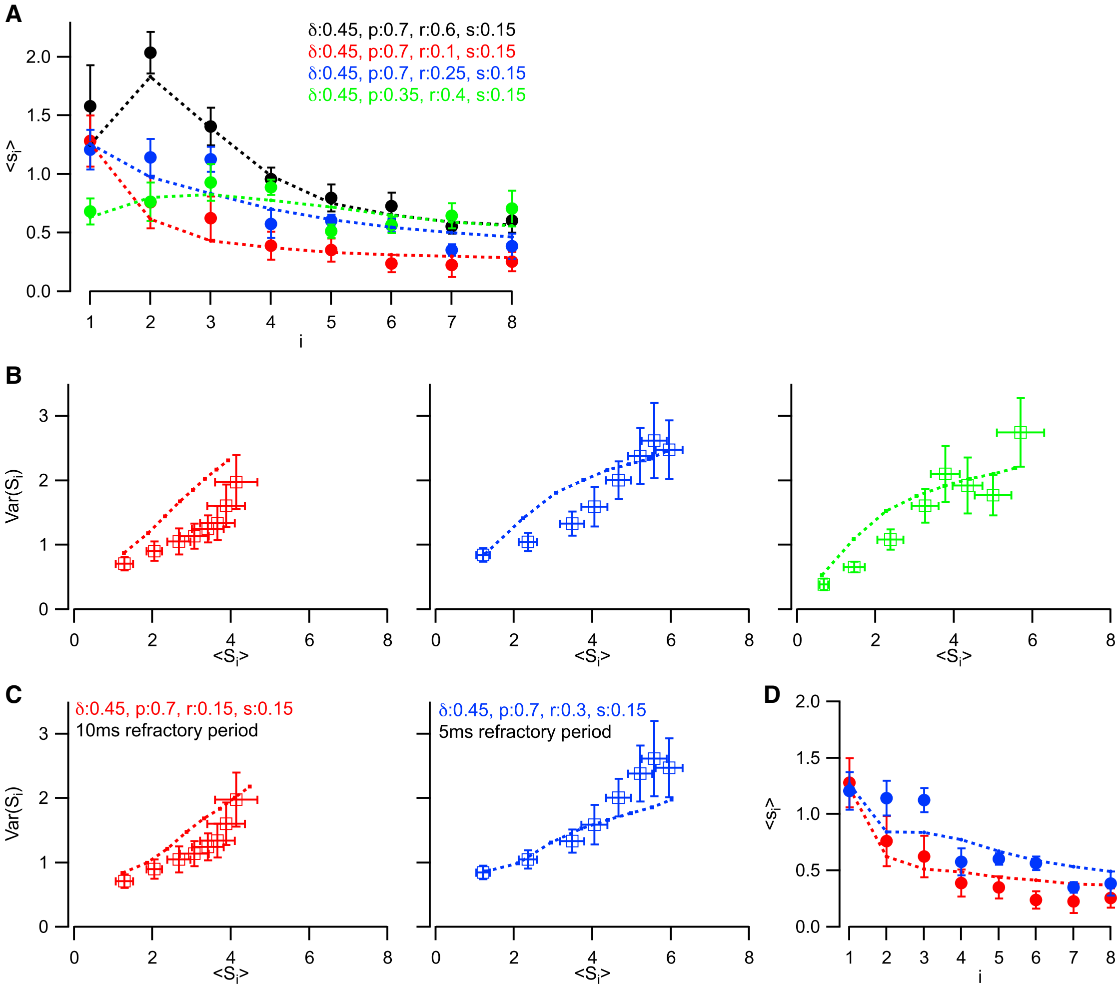

Figure 6. Simulation of Pharmacological Experiments

Monte Carlo simulations using the two-step model (as in Figure 2E) with $N_1 = 4$. Control parameters are as follows: $\delta = 0.45$, $p = 0.7$, $r = 0.6$, and $s = 0.15$ (black). Reducing r to 0.1 and 0.25, respectively, mimics latrunculin B (red) and blebbistatin results (blue). Reducing both p (to 0.35) and r (to 0.4) mimics EGTA results (green).

(A) s_i curves. Simulations (dashed lines) mimic the facilitation/depression sequence observed in control, the gradual depression observed in latrunculin B and blebbistatin, and the almost stable s_i curve observed in EGTA.

(B) var (S_i) versus $<S_i>$ curves for the three conditions (squares, group data; dashed lines, simulations).

(C) A refractory period was simulated after each release event, prohibiting docking site reoccupation during 10 ms (in latrunculin B) or 5 ms (in blebbistatin). Least-squares fits (continuous lines) of var (S_i) versus $<S_i>$ curves in latrunculin B and in blebbistatin gave r = 0.15 (left) and r = 0.3 (right).

(D) Corresponding $<s_i>$ curves are close to experimental data.

facilitation is abolished. This suggests a model of facilitation based on increased docking site occupancy rather than on increased probability of exocytosis of docked vesicles.

Two-Step Approach to Exocytosis

The two-step model is illustrated in Figure 8A for a simple synapse with four docking sites. It posits that empty docking sites are not directly replenished from a large pool, as is commonly assumed, but from a small, most probably very local pool of replacement SVs. (Note that in Figure 8, we arbitrarily drew replacement SVs on top of docked SVs, but that an equally likely location would be on the side of docked SVs, in contact with the plasma membrane.) A first line of evidence in favor of this model comes from the variance data illustrated in Figure 1 together with their simulation, as shown in Figure 2. A second line of evidence in favor of the two-step model comes from pharmacological perturbations, particularly with latrunculin B and blebbistatin (Figures 5 and 6). The finding that these actin- and myosin-disrupting drugs primarily target the replacement step suggests that this step reflects an active cytoskeleton-driven vesicle movement.

RRP, Docked SVs, and Replacement SVs

Whether replacement SVs belong to the RRP or not depends on the definition that is adopted for the RRP. If the RRP is taken in its strictest sense, as the maximum number of SVs that can be delivered by 1 AP, then only docked SVs constitute the RRP,

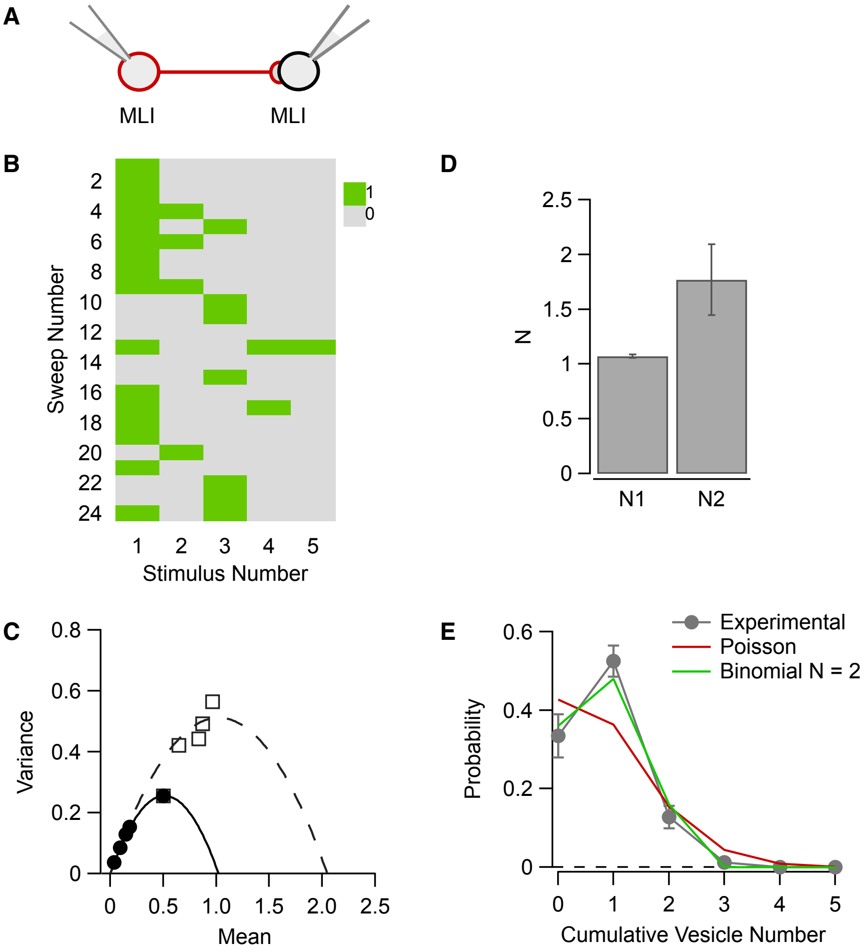

Figure 7. Statistics of Cumulative Released Vesicle Numbers in Elementary GABAergic Synapses

(A) Paired recordings were obtained from synaptically connected MLIs. In some cases, these connections involve simple synapses having a single docking site; such connections are called "elementary synapses" (Pulido et al., 2015). Trains of 5 APs were applied at a frequency of 25 Hz, with 10 s waiting times between trains.

(B) Patterns of success/failures for a representative experiment. Note that 1 SV is maximally released following each AP.

(C) Plots of var (s_i) a function of $<s_i>$ (filled circles; parabolic fit yields $N_1 = 1.0$) and of var (S_i) as a function of $<S_i>$ (open squares; parabolic fit yields $N_2 = 2.0$), from the experiment shown in (B) (total number of trains, 54).

(D) Group results showing means of N_1 and N_2 values (m. ± SEM) across elementary synapses (n = 7).

(E) Distribution of $P(S_5)$ values for seven elementary synapses, showing an abrupt fall for 3 SVs. A Poisson distribution with same mean as that of $P(S_5)$ (red) and a binomial distribution with N = 2, p = 0.40 (green), are shown for comparison.

with total number δN_1. Since the mean value of N_1 is 5.2 (Figure 1G), and our best estimate of δ is 0.45, this first definition gives a mean RRP size of 0.45 per docking site, and of 0.45 × 5.2 = 2.34 per active zone. If, however, the RRP is taken as the sum of docked and replacement SVs initially present, we obtain 1.45 per docking site (assuming an initial occupancy of the replacement site of 1) and 1.45 × 5.2 = 7.54 per active zone. Finally, if the RRP is estimated by linear extrapolation of the cumulative release plot, an intermediate value is obtained (4.6 per active zone in experimental data, Figure 1I; 4.8 per active zone in simulations, Figure 8B; this corresponds to a RRP size per docking site of 4.8/5.2 = 0.92). According to the analysis by Neher (2015), such a plot reports the sum of decrements in pool sizes during trains. For the two-step model, this involves both docked and replacement pools, which together lose 1.09 SV per docking site, since the sum ($\rho + \delta$) is 1.45 before the train and drops to 0.36 at steady state (Figures 8C and 8D); this total loss is close to the expected value of 0.92. Thus, while the extrapolation method comes up with a RRP size around 1 SV per site, the more detailed analysis of Figure 8B suggests that only part of this value represents SVs that had been originally docked at the active zone, the rest being recruited from the replacement pool during the dynamic phase of responses to stimulus trains.

Possible Morphological Correlates of Docked and Replacement SVs

Studies using super-resolution optical microscopy (Matkovic et al., 2013) and electron microscopy (Hirokawa et al., 1989; Siksou et al., 2009; Fernández-Busnadiego et al., 2010; Szule et al., 2012; Imig et al., 2014) indicate a highly organized arrangement of SVs and of cytoskeletal elements in a variety of synapses. In each active zone, a small number of docked SVs are directly in contact with the plasma membrane, where they are associated with specific cytomatrix proteins (Matkovic et al., 2013). In some cases, another set of SVs is less directly associated to the docking site. In the frog neuromuscular junction, these SVs are located deeper in the cytosol, behind the docked SVs (Szule et al., 2012). In the mouse neuromuscular junction, the supplementary SVs are located on the side of primary docked vesicles, close to the plasma membrane (Nagwaney et al., 2009). In the frog and mouse neuromuscular junctions, both primary and secondary docked SVs are linked to the plasma membrane by specific cytoskeletal elements. These results are consistent with the coexistence of two kinds of SVs differentially poised for exocytosis.

Docking Site Occupancy

We find that the docking site occupancy δ is less than 1 at rest, in agreement with earlier work at GABAergic synapses (Trigo et al., 2012; Pulido et al., 2015). δ is governed by two rate constants, p and r, which are both increased during the train, as they are both Ca^{2+} dependent. Our results and simulations do not address the values of p or r before the train, so that it is unclear what determines the basal value of δ. It is possible that in the

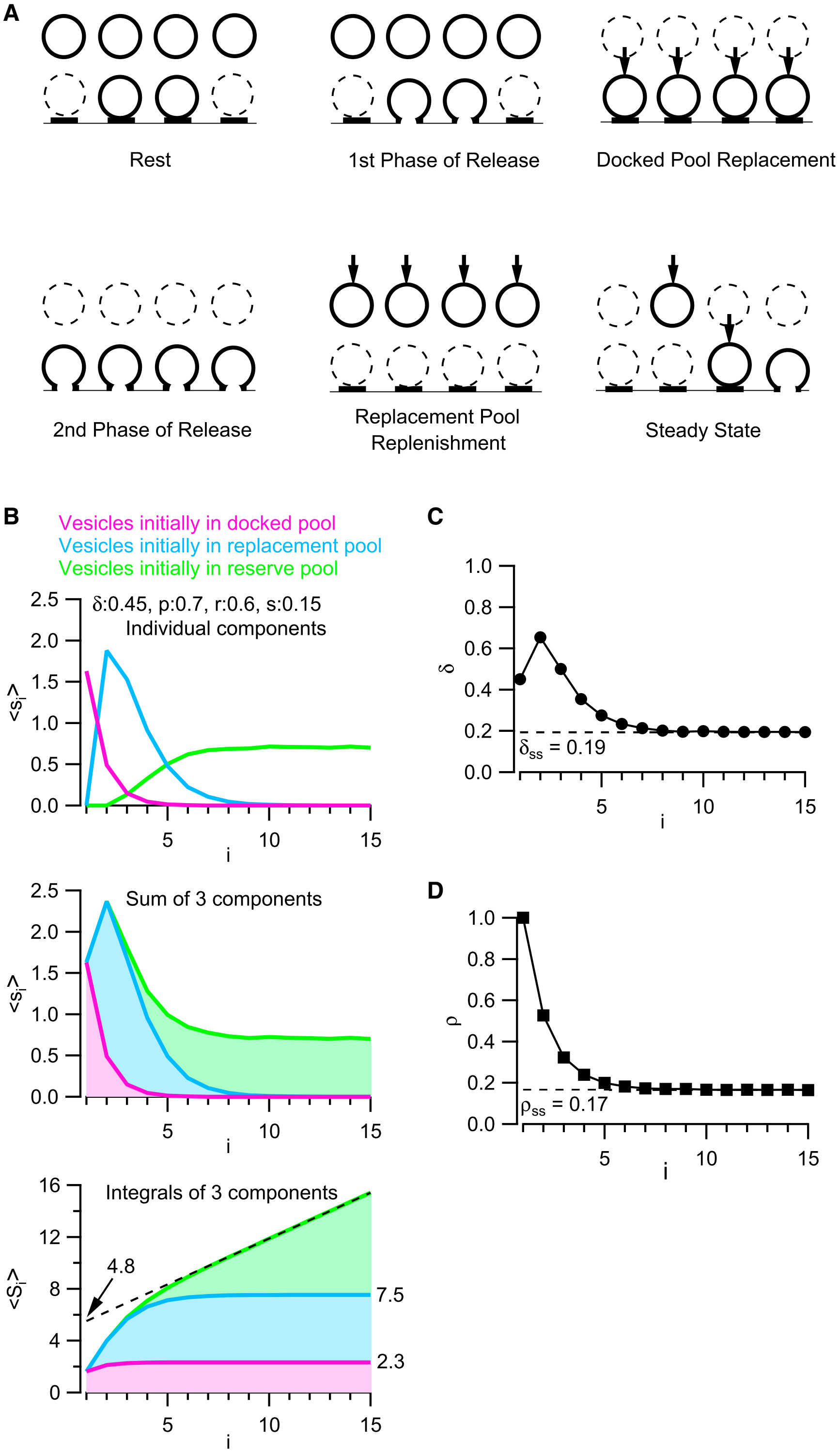

Figure 8. The Various Phases of Vesicular Release in the Two-Step Model

Monte Carlo simulations are presented, assuming the two-step model with $\delta = 0.45$, $p = 0.7$, $r = 0.6$, $s = 0.15$, as in Figures 2F and 2G.

(A) Schematics of the various phases of vesicular release for a synapse containing four docking sites. At rest about half of the docking sites are occupied, but all replacement sites are occupied. Following exocytosis of docked SVs (first phase of release), the docked pool increases rapidly, giving rise to a large second phase of release (facilitation). Later in the train, slow replenishment of the replacement pool limits steady-state release.

(B) For each release event during an AP train, the origin of the released SV was traced back to the onset of the train. In this manner, the contributions of SVs initially belonging to the docked pool (red), to the replacement pool (blue), and to the recycling pool (green) were determined. Results were scaled to an average number of docking sites of 5.2. (Upper panel) Contributions of each SV population to the $<s_i>$ plot. (Middle panel) Each component is shown as a shaded area with appropriate color together with the sum of the 3. Like in the data of Figure 5A, this sum follows a potentiating/depressing time course. (Lower panel) As in the middle panel, now showing cumulative release. Three different estimates of the RRP size are illustrated: by back extrapolation of the S_i curve, giving 4.8; by summing the docked SV component, giving 2.3; and by summing the docked and replacement SV components, giving 7.5. Corresponding RRP sizes per docking site are, respectively, 0.92, 0.45, and 1.45.

(C) Plot of docking site occupancy versus stimulus number, showing a peak during facilitation.

(D) Plot of replacement site occupancy versus stimulus number, exhibiting monotonous decrease. Note that the sum ($\rho + \delta$) drops from 1.45 before the train to 0.36 at steady state.

basal state the replacement step is reversible, adding a backward step in parallel with r (Midorikawa and Sakaba, 2015). It is also possible that steric hindrance between SVs attached to neighboring docking sites prevents δ from reaching 1 under basal conditions.

Implications for Synaptic Facilitation

Current models of synaptic facilitation usually assume that "residual calcium," the spatially averaged Ca^{2+} signal resulting from Ca^{2+} entry after dissipation of submicron gradients, increases the probability of exocytosis of SVs belonging to the RRP (Zucker et al., 2009). Several mechanisms of action of residual calcium have been proposed, including facilitation of Ca^{2+} currents (Hori and Takahashi, 2009); however, at PF-MLI synapses, Ca^{2+} imaging data do not support this mechanism (Brenowitz and Regehr, 2007; Figure 3). The two-step model suggests a mechanism of synaptic facilitation that has received little attention until now. We find that $\delta < 1$ at rest, and furthermore that SV replenishment of emptied docking sites can be fast enough to significantly increase docking site occupancy with interpulse intervals as short as 5 ms. With these two notions, a natural explanation of facilitation is an increase of δ with stimulus number (Figure 8C) at the expense of the replacement pool (Figure 8D). This view does not preclude the possibility of a change of the probability of exocytosis p by some other mechanism. A similar hypothesis has been proposed earlier to explain facilitation at tonic crayfish synapses (Pan and Zucker, 2009). In our simulations (Figure 8B), responses during a train proceed sequentially from SVs located at stimulus onset in the docked vesicle pool (i = 1–3), in the replacement pool (i = 2–5), and in the recycling pool ($i \geq 5$). It is the transient swell of the contribution of replacement SVs during stimuli 2–5 that accounts for facilitation in this model. Thus replacement SVs are ideally poised to maintain EPSPs in response to short AP bursts at high frequency, as exhibited by PFs in vivo (Chadderton et al., 2004). In summary, the scheme of Figure 8 shows the feasibility of a model of facilitation based on changes of δ rather than on changes of p.

EXPERIMENTAL PROCEDURES

Single synapse recordings were obtained in cerebellar MLIs (either stellate or basket cells) as described (Malagon et al., 2016). Experiments were performed at 30°C–34°C in cerebellar slices from rats aged 13–16 days. Details are given in the Supplemental Experimental Procedures.

SUPPLEMENTAL INFORMATION

Supplemental Information includes seven figures and Supplemental Experimental Procedures and can be found with this article online at http://dx.doi.org/10.1016/j.neuron.2016.07.033.

AUTHOR CONTRIBUTIONS

T.M., G.M., C.P., and I.L. conducted the experiments. I.L., E.N., and A.M. designed the experiments and wrote the paper. T.M., G.M., C.P., I.L. and E.N. designed analysis procedures and performed analysis.

ACKNOWLEDGMENTS

This work was supported by an ERC Advanced grant (“SingleSite”) to A.M. and benefited from a JSPS Core-to-Core Program A (Advanced Research Networks). We thank Brandon Stell and Federico Trigo for comments on the manuscript.

Received: January 6, 2016
Revised: May 17, 2016
Accepted: July 11, 2016
Published: August 17, 2016

REFERENCES

Atluri, P.P., and Regehr, W.G. (1998). Delayed release of neurotransmitter from cerebellar granule cells. J. Neurosci. *18*, 8214–8227.

Bao, J., Reim, K., and Sakaba, T. (2010). Target-dependent feedforward inhibition mediated by short-term synaptic plasticity in the cerebellum. J. Neurosci. *30*, 8171–8179.

Bender, V.A., Pugh, J.R., and Jahr, C.E. (2009). Presynaptically expressed long-term potentiation increases multivesicular release at parallel fiber synapses. J. Neurosci. *29*, 10974–10978.

Bollmann, J.H., Sakmann, B., and Borst, J.G. (2000). Calcium sensitivity of glutamate release in a calyx-type terminal. Science *289*, 953–957.

Brenowitz, S.D., and Regehr, W.G. (2007). Reliability and heterogeneity of calcium signaling at single presynaptic boutons of cerebellar granule cells. J. Neurosci. *27*, 7888–7898.

Chadderton, P., Margrie, T.W., and Häusser, M. (2004). Integration of quanta in cerebellar granule cells during sensory processing. Nature *428*, 856–860.

Clements, J.D. (2003). Variance-mean analysis: a simple and reliable approach for investigating synaptic transmission and modulation. J. Neurosci. Methods *130*, 115–125.

Cole, J.C., Villa, B.R., and Wilkinson, R.S. (2000). Disruption of actin impedes transmitter release in snake motor terminals. J. Physiol. *525*, 579–586.

Crowley, J.J., Carter, A.G., and Regehr, W.G. (2007). Fast vesicle replenishment and rapid recovery from desensitization at a single synaptic release site. J. Neurosci. *27*, 5448–5460.

Eggermann, E., Bucurenciu, I., Goswami, S.P., and Jonas, P. (2011). Nanodomain coupling between Ca^{2+} channels and sensors of exocytosis at fast mammalian synapses. Nat. Rev. Neurosci. *13*, 7–21.

Fernández-Busnadiego, R., Zuber, B., Maurer, U.E., Cyrklaff, M., Baumeister, W., and Lucic, V. (2010). Quantitative analysis of the native presynaptic cytomatrix by cryoelectron tomography. J. Cell Biol. *188*, 145–156.

Hallermann, S., and Silver, R.A. (2013). Sustaining rapid vesicular release at active zones: potential roles for vesicle tethering. Trends Neurosci. *36*, 185–194.

Hayashida, M., Tanifuji, S., Ma, H., Murakami, N., and Mochida, S. (2015). Neural activity selects myosin IIB and VI with a specific time window in distinct dynamin isoform-mediated synaptic vesicle reuse pathways. J. Neurosci. *35*, 8901–8913.

Hirokawa, N., Sobue, K., Kanda, K., Harada, A., and Yorifuji, H. (1989). The cytoskeletal architecture of the presynaptic terminal and molecular structure of synapsin 1. J. Cell Biol. *108*, 111–126.

Hori, T., and Takahashi, T. (2009). Mechanisms underlying short-term modulation of transmitter release by presynaptic depolarization. J. Physiol. *587*, 2987–3000.

Hosoi, N., Sakaba, T., and Neher, E. (2007). Quantitative analysis of calcium-dependent vesicle recruitment and its functional role at the calyx of Held synapse. J. Neurosci. *27*, 14286–14298.

Hosoi, N., Holt, M., and Sakaba, T. (2009). Calcium dependence of exo- and endocytotic coupling at a glutamatergic synapse. Neuron *63*, 216–229.

Imig, C., Min, S.-W., Krinner, S., Arancillo, M., Rosenmund, C., Südhof, T.C., Rhee, J., Brose, N., and Cooper, B.H. (2014). The morphological and molecular nature of synaptic vesicle priming at presynaptic active zones. Neuron *84*, 416–431.

Ishiyama, S., Schmidt, H., Cooper, B.H., Brose, N., and Eilers, J. (2014). Munc13-3 superprimes synaptic vesicles at granule cell-to-basket cell synapses in the mouse cerebellum. J. Neurosci. *34*, 14687–14696.

Lee, J.S., Ho, W.-K., and Lee, S.-H. (2012). Actin-dependent rapid recruitment of reluctant synaptic vesicles into a fast-releasing vesicle pool. Proc. Natl. Acad. Sci. USA *109*, E765–E774.

Malagon, G., Miki, T., Llano, I., Neher, E., and Marty, A. (2016). Counting vesicular release events reveals binomial release statistics at single glutamatergic synapses. J. Neurosci. *36*, 4010–4025.

Matkovic, T., Siebert, M., Knoche, E., Depner, H., Mertel, S., Owald, D., Schmidt, M., Thomas, U., Sickmann, A., Kamin, D., et al. (2013). The Bruchpilot cytomatrix determines the size of the readily releasable pool of synaptic vesicles. J. Cell Biol. *202*, 667–683.

Midorikawa, M., and Sakaba, T. (2015). Imaging exocytosis of single synaptic vesicles at a fast CNS presynaptic terminal. Neuron *88*, 492–498.

Mochida, S., Kobayashi, H., Matsuda, Y., Yuda, Y., Muramoto, K., and Nonomura, Y. (1994). Myosin II is involved in transmitter release at synapses formed between rat sympathetic neurons in culture. Neuron *13*, 1131–1142.

Morales, M., Colicos, M.A., and Goda, Y. (2000). Actin-dependent regulation of neurotransmitter release at central synapses. Neuron *27*, 539–550.

Nagwaney, S., Harlow, M.L., Jung, J.H., Szule, J.A., Ress, D., Xu, J., Marshall, R.M., and McMahan, U.J. (2009). Macromolecular connections of active zone material to docked synaptic vesicles and presynaptic membrane at neuromuscular junctions of mouse. J. Comp. Neurol. *513*, 457–468.

Neher, E. (2010). What is rate-limiting during sustained synaptic activity: vesicle supply or the availability of release sites. Front. Synaptic Neurosci. *2*, 144.

Neher, E. (2015). Merits and limitations of vesicle pool models in view of heterogeneous populations of synaptic vesicles. Neuron *87*, 1131–1142.

Neher, E., and Sakaba, T. (2008). Multiple roles of calcium ions in the regulation of neurotransmitter release. Neuron *59*, 861–872.

Pan, B., and Zucker, R.S. (2009). A general model of synaptic transmission and short-term plasticity. Neuron *62*, 539–554.

Pulido, C., Trigo, F.F., Llano, I., and Marty, A. (2015). Vesicular release statistics and unitary postsynaptic current at single GABAergic synapses. Neuron *85*, 159–172.

Ritzau-Jost, A., Delvendahl, I., Rings, A., Byczkowicz, N., Harada, H., Shigemoto, R., Hirrlinger, J., Eilers, J., and Hallermann, S. (2014). Ultrafast action potentials mediate kilohertz signaling at a central synapse. Neuron *84*, 152–163.

Rizzoli, S.O., and Betz, W.J. (2005). Synaptic vesicle pools. Nat. Rev. Neurosci. *6*, 57–69.

Ruiz, R., Cano, R., Casañas, J.J., Gaffield, M.A., Betz, W.J., and Tabares, L. (2011). Active zones and the readily releasable pool of synaptic vesicles at the neuromuscular junction of the mouse. J. Neurosci. *31*, 2000–2008.

Ryan, T.A. (1999). Inhibitors of myosin light chain kinase block synaptic vesicle pool mobilization during action potential firing. J. Neurosci. *19*, 1317–1323.

Sakaba, T. (2006). Roles of the fast-releasing and the slowly releasing vesicles in synaptic transmission at the calyx of Held. J. Neurosci. *26*, 5863–5871.

Sakaba, T., and Neher, E. (2001). Calmodulin mediates rapid recruitment of fast-releasing synaptic vesicles at a calyx-type synapse. Neuron *32*, 1119–1131.

Sakaba, T., and Neher, E. (2003). Involvement of actin polymerization in vesicle recruitment at the calyx of Held synapse. J. Neurosci. *23*, 837–846.

Sankaranarayanan, S., Atluri, P.P., and Ryan, T.A. (2003). Actin has a molecular scaffolding, not propulsive, role in presynaptic function. Nat. Neurosci. *6*, 127–135.

Satake, S., Inoue, T., and Imoto, K. (2012). Paired-pulse facilitation of multivesicular release and intersynaptic spillover of glutamate at rat cerebellar granule cell-interneurone synapses. J. Physiol. *590*, 5653–5675.

Saviane, C., and Silver, R.A. (2006). Fast vesicle reloading and a large pool sustain high bandwidth transmission at a central synapse. Nature *439*, 983–987.

Scheuss, V., and Neher, E. (2001). Estimating synaptic parameters from mean, variance, and covariance in trains of synaptic responses. Biophys. J. *81*, 1970–1989.

Scheuss, V., Schneggenburger, R., and Neher, E. (2002). Separation of presynaptic and postsynaptic contributions to depression by covariance analysis of successive EPSCs at the calyx of Held synapse. J. Neurosci. *22*, 728–739.

Schneggenburger, R., and Neher, E. (2000). Intracellular calcium dependence of transmitter release rates at a fast central synapse. Nature *406*, 889–893.

Schneggenburger, R., Meyer, A.C., and Neher, E. (1999). Released fraction and total size of a pool of immediately available transmitter quanta at a calyx synapse. Neuron *23*, 399–409.

Siksou, L., Varoqueaux, F., Pascual, O., Triller, A., Brose, N., and Marty, S. (2009). A common molecular basis for membrane docking and functional priming of synaptic vesicles. Eur. J. Neurosci. *30*, 49–56.

Silver, R.A., Lubke, J., Sakmann, B., and Feldmeyer, D. (2003). High-probability uniquantal transmission at excitatory synapses in barrel cortex. Science *302*, 1981–1984.

Srinivasan, G., Kim, J.H., and von Gersdorff, H. (2008). The pool of fast releasing vesicles is augmented by myosin light chain kinase inhibition at the calyx of Held synapse. J. Neurophysiol. *99*, 1810–1824.

Szule, J.A., Harlow, M.L., Jung, J.H., De-Miguel, F.F., Marshall, R.M., and McMahan, U.J. (2012). Regulation of synaptic vesicle docking by different classes of macromolecules in active zone material. PLoS ONE *7*, e33333.

Takagishi, Y., Futaki, S., Itoh, K., Espreafico, E.M., Murakami, N., Murata, Y., and Mochida, S. (2005). Localization of myosin II and V isoforms in cultured rat sympathetic neurones and their potential involvement in presynaptic function. J. Physiol. *569*, 195–208.

Taschenberger, H., Scheuss, V., and Neher, E. (2005). Release kinetics, quantal parameters and their modulation during short-term depression at a developing synapse in the rat CNS. J. Physiol. *568*, 513–537.

Trigo, F.F., Sakaba, T., Ogden, D., and Marty, A. (2012). Readily releasable pool of synaptic vesicles measured at single synaptic contacts. Proc. Natl. Acad. Sci. USA *109*, 18138–18143.

Valera, A.M., Doussau, F., Poulain, B., Barbour, B., and Isope, P. (2012). Adaptation of granule cell to Purkinje cell synapses to high-frequency transmission. J. Neurosci. *32*, 3267–3280.

Zucker, R.S., Kullmann, D.M., and Schwarz, T.L. (2009). Release of neurotransmitters. In From Molecules to Networks, J.H. Byrne and J.L. Roberts, eds. (Sinauer), pp. 217–266.

Neuron, Volume *91*

Supplemental Information

Actin- and Myosin-Dependent Vesicle Loading of Presynaptic Docking Sites Prior to Exocytosis

Takafumi Miki, Gerardo Malagon, Camila Pulido, Isabel Llano, Erwin Neher, and Alain Marty

Supplemental Information

Inventory of Supplemental Information

Supplemental Information contains 7 Supplemental Figures, followed by Supplemental Experimental Procedures, and by Supplemental References.

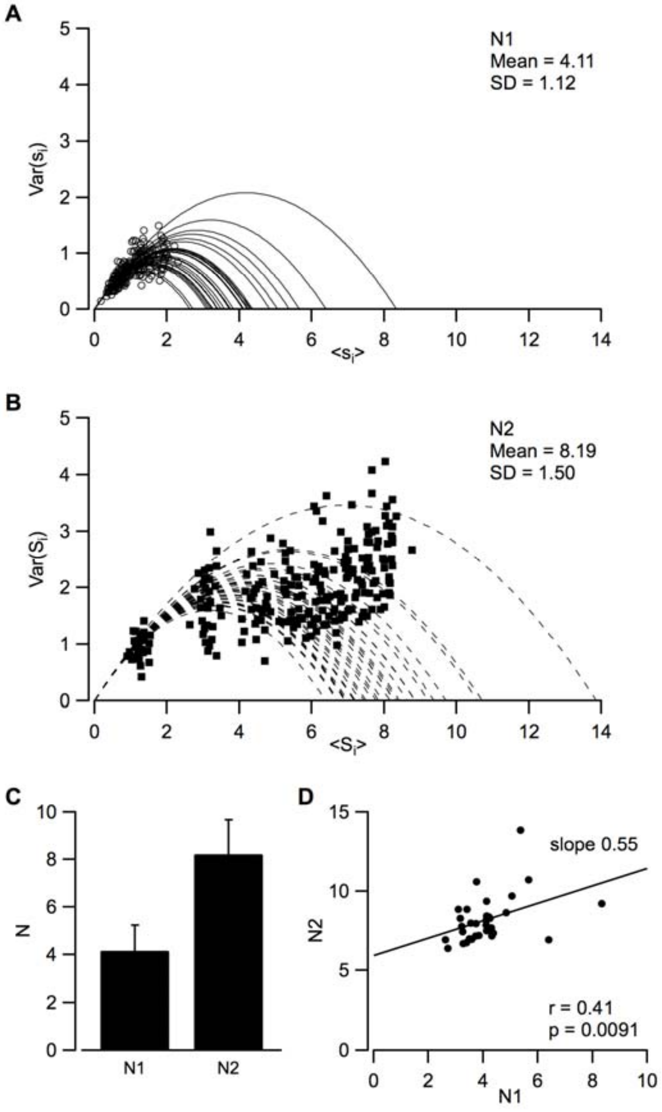

Figure S1, related to Figures 1 and 2: Stochastic uncertainty on the determination of N_1 and N_2
Monte Carlo simulations were performed mimicking 30-trial experiments with $N_1 = 4$, $N_2 = 8$ (renewable 2-step model giving the best least-squares score for control data: $\delta = 0.45$, $p = 0.7$, $r = 0.6$, $s = 0.15$).

A, B: In each simulated experiment, N_1 and N_2 were obtained from parabolic fits to synchronized (A: circles, simulated variance/mean points for individual stimulations; continuous lines, corresponding parabolic fits) and cumulative (B: squares and dotted lines) variance plots.

C: Mean and SD of N_1 and N_2 values resulting from individual simulations.

D: Plot of N_2 vs. N_1 in individual simulations reveals a significant correlation. This results from the link between s_i and S_i values in individual trials: large s_i values (generated by stochastic fluctuations) tend to yield both large N_1 and large N_2 estimates. However the corresponding Pearson's coefficient ($r = 0.41$), as well as the slope of the regression line (0.55), are markedly weaker than experimentally observed (respectively 0.81 and 1.63; Fig. 1H).

Overall the present analysis suggests that part of the variations of N_1 and N_2 determined in individual experiments arise from statistical fluctuations linked to the finite number of trials that were recorded (usually 30). However the finding of larger values for Pearson's coefficient, as well as for the slope of the regression line, in Fig. 1H (experimental) compared with panel D (simulations), suggests that the observed correlation between N_1 and N_2 exceeds the correlation expected from statistical fluctuations, and mainly originates from genuine differences among simple synapses.

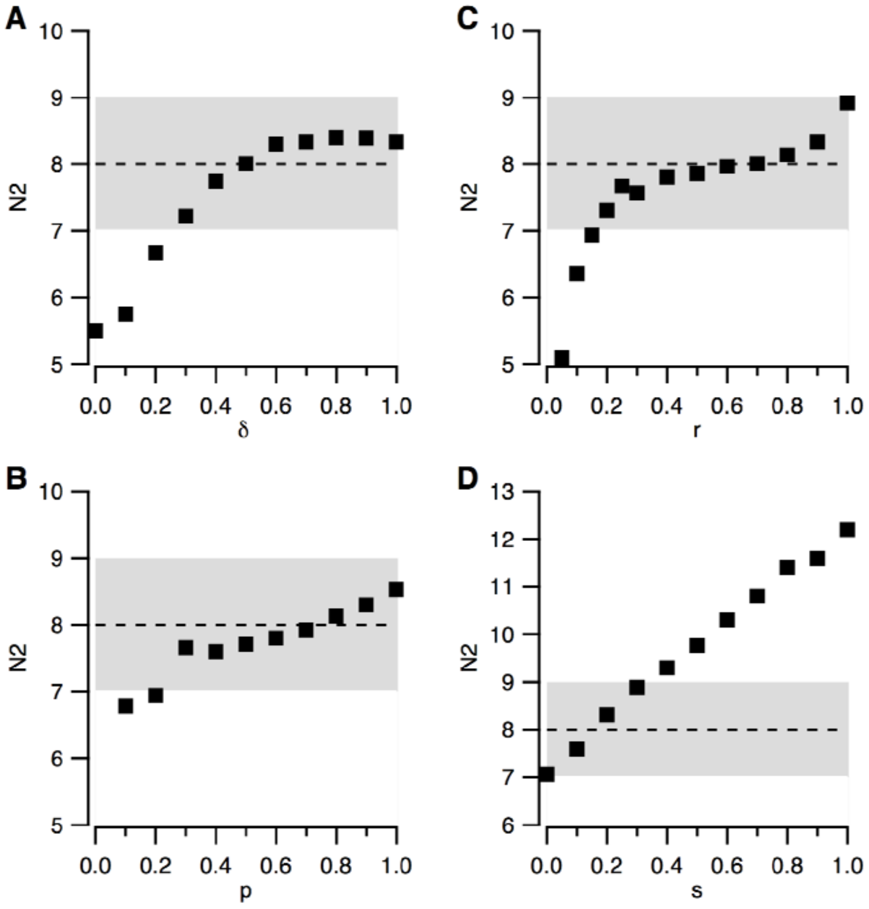

Figure S2, related to Figure 2: Effect of varying δ, p, r or s on estimate of N_2
Monte Carlo simulations were run as in Fig. 2E, based on the renewable 2-step model giving the best least-squares score for control data: $\delta = 0.45$, $p = 0.7$, $r = 0.6$, $s = 0.15$. 3 of the parameters were kept identical to this reference case, and the 4th parameter was altered between 0 and 1. For each new value of the altered parameter the corresponding value of N_2 was determined by using the parabolic plot of cumulative variance. In each plot a band indicates a range of N_2 values ($7 \leq N_2 \leq 9$) considered reasonably close to the ideal value $N_2 = 8$.
A: The condition ($7 \leq N_2 \leq 9$) was fulfilled for δ values ranging from 0.3 to 1.
B: The condition ($7 \leq N_2 \leq 9$) was fulfilled for p values ranging from 0.3 to 1.
C: The condition ($7 \leq N_2 \leq 9$) was fulfilled for r values ranging from 0.2 to 1.
D: The condition ($7 \leq N_2 \leq 9$) was fulfilled for s values ranging from 0 to 0.3.

These plots show that approximately correct N_2 values are obtained for large ranges of model parameters. However large deviations are predicted for very low δ or r values, as well as for s values larger than 0.3.

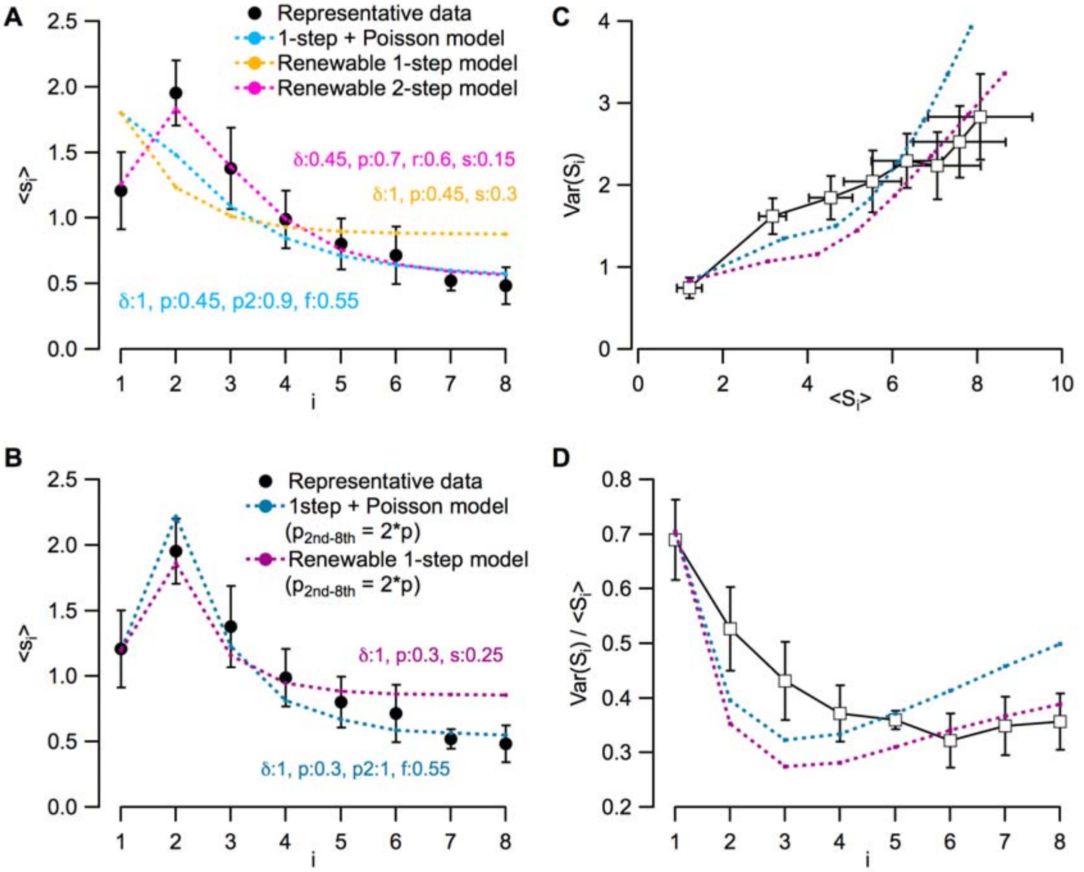

Figure S3, related to Figure 2: Simulation of 1-step models with variable p values

A: $\langle s_i \rangle$ curves corresponding to the best parameter sets from Fig. 2F, for the 2-step model (red), for the 1-step + Poisson model (blue), and for the renewable 1-step model (orange), are compared to experimental data (black). Here p is constant for all models, and only the 2-step model approaches the data.

B-D: After imposing a 2-fold ratio for p between the first and the second stimulus ($p_i/p_1 = 2$ for i = 2-8), $\langle s_i \rangle$ curves for the 2 variants of the 1-step model become closer to experimental data (**B**). However, even after readjustment of the parameter sets to minimize summed squared deviations, both 1-step models fail to account for the experimental var (S_i) curve (**C**) or for the var (S_i) / $\langle S_i \rangle$ curve (**D**).

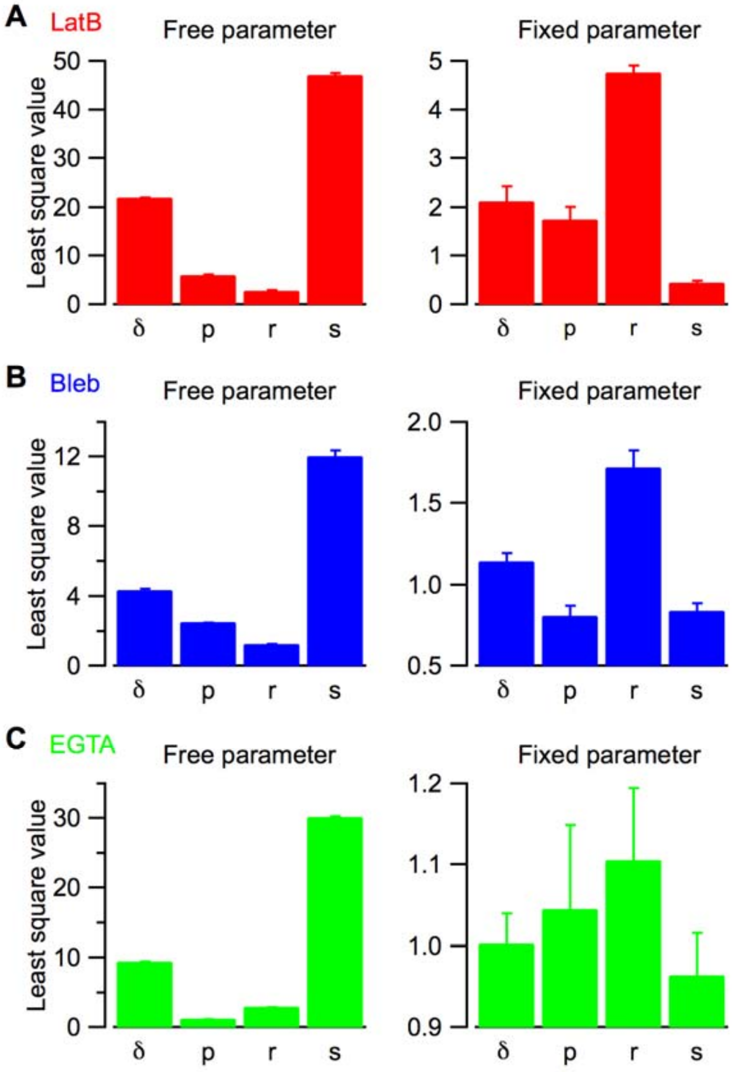

Figure S4, related to Figure 5: Least-squares scores of simulations of experiments with latrunculin B, blebbistatin and EGTA

The reference simulation is the 2-step model of Fig. 2E with the set of parameters giving the best least-squares score for control data: δ = 0.45, p = 0.7, r = 0.6, s = 0.15. Left column: Starting with these values, simulations of var (S_i) curves were run keeping 3 parameters fixed at these control values and leaving 1 free. The least-squares score is then plotted as a function of the parameter that is varied. Right column: Simulations were now run keeping 1 parameter fixed and leaving 3 free. The least-squares score is then plotted as a function of the parameter that is fixed. Low scores in the left column, and/or high scores in the right column, indicate that changing the corresponding parameter is important in achieving a good model of the examined pharmacological effect.

A: Latrunculin B experiments. r gives the lowest score in the free parameter test (left), and the highest score in the fixed parameter test (right). This indicates that a change in r is the principal factor determining the effects of latrunculin B.

B: Blebbistatin experiments. Again r appears as the principal parameter determining the effects of blebbistatin.

C: EGTA experiments. Changes in parameters p and r contribute strongly to determine the effects of EGTA, while parameters δ and s appear less important.

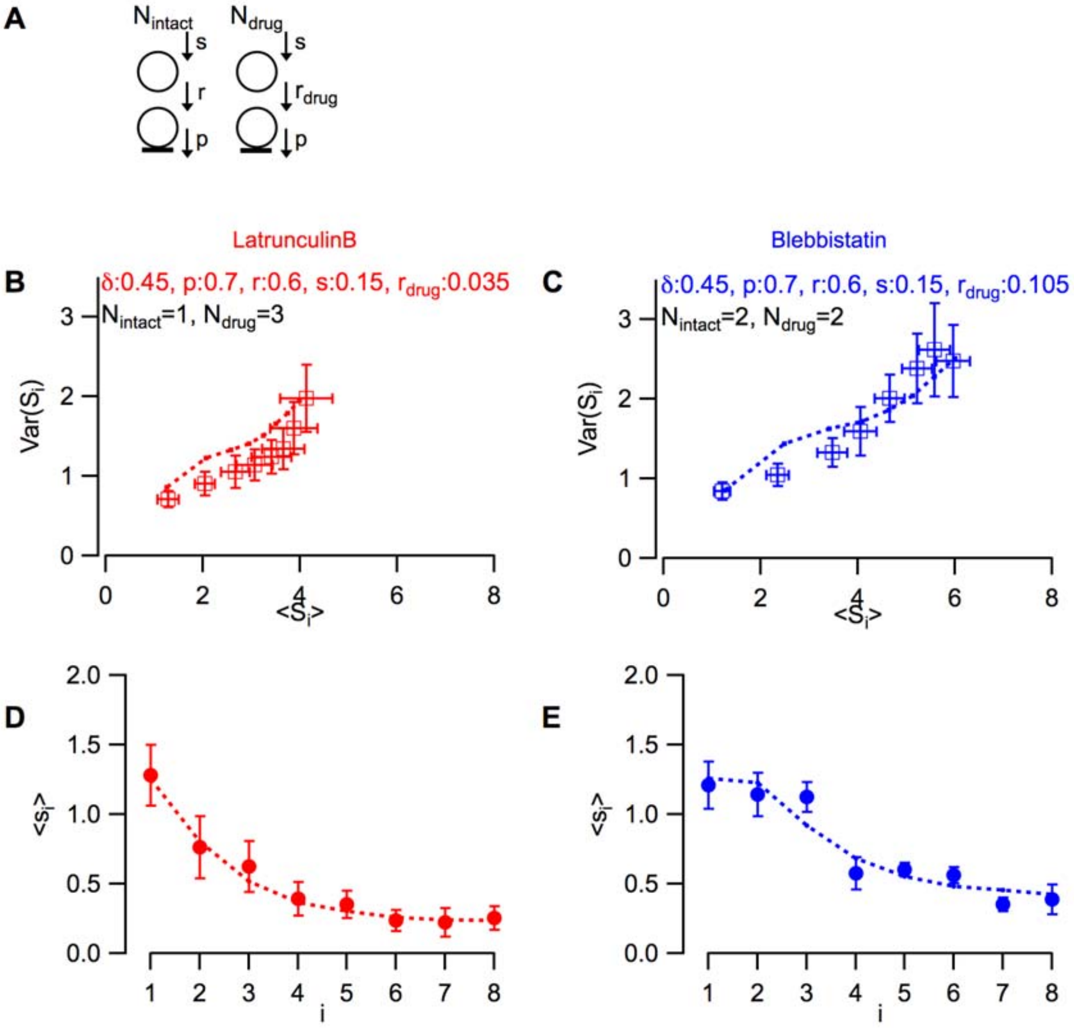

Figure S5, related to Figure 6: Simulation of heterogeneous latrunculin B and blebbistatin effects

A: Here we assume that some of the docking sites continue to operate normally (N_{intact} = 1 in latrunculin B, and N_{intact} = 2 in blebbistatin), while the other docking sites have a much reduced r value (0.035 in latrunculin, and 0.105 in blebbistatin).

B, C: var (S_i) vs. <S_i> curves in latrunculin B and in blebbistatin (squares: grouped data; dashed lines: simulations). Fits are closer to experimental data than in Fig. 6B.

D, E: Same for <s_i> curves.

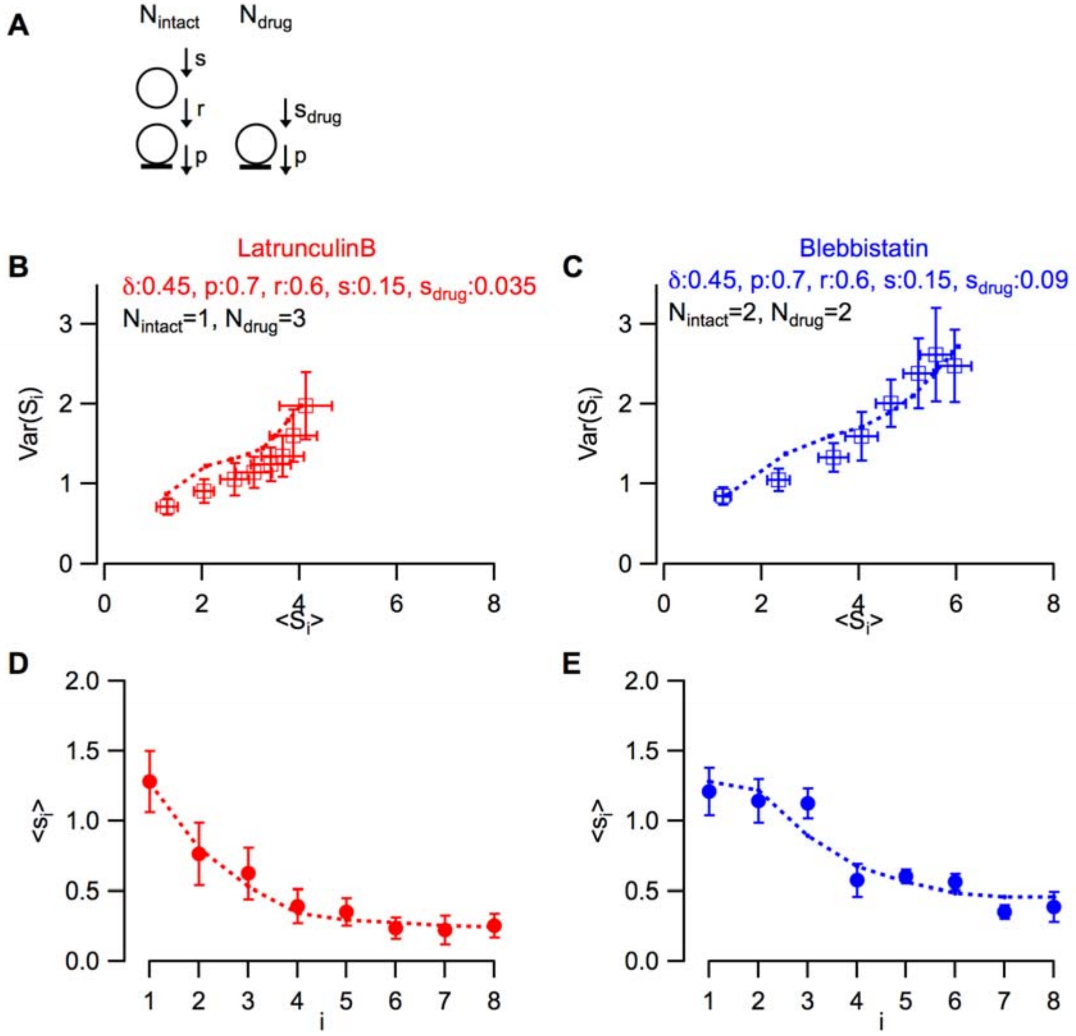

Figure S6, related to Figure 6: Simulation of latrunculin B experiments and of blebbistatin experiments, assuming an elimination of replacement sites

A: In these simulations, like in Fig. S5, some docking sites remain intact during parmacological treatment (1 in latrunculin B, 2 in blebbistatin). Other docking sites lose their associated replacement site, and are directly replenished from a large vesicular pool with a new rate constant s_{drug}, smaller than s.

B, C: Least-squares fits of var (S_i) vs. $<S_i>$ curves in latrunculin B and in blebbistatin respectively gave s_{drug} = 0.035 (**B**) and s_{drug} = 0.09 (**C**).

D, E: Corresponding $<s_i>$ curves are close to experimental data.

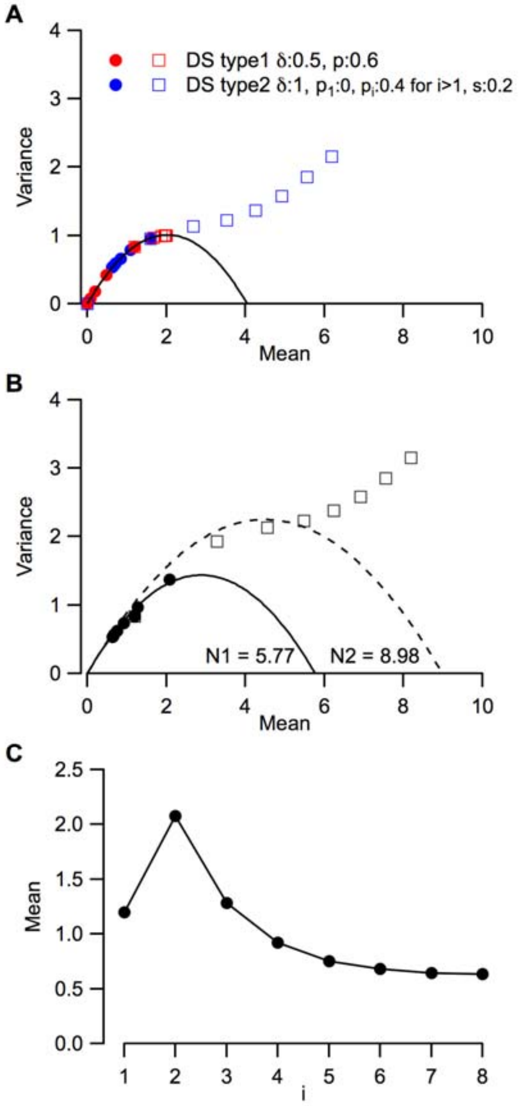

Figure S7, related to Figure 6: Simulation of two different populations of docking sites

In this simulation two sets of docking sites are assumed to coexist in the same active zone. First, 4 docking sites follow a 1-step docking site model without replenishment. They primarily contribute to the responses observed in the beginning of the train, particularly in response to the 1st and 2nd stimuli. A second set of 4 docking sites follow a 1-step docking site model with replenishment. These docking sites are assumed to be totally silent in response to the 1st stimulus, and to be turned on with a fixed p value starting with the 2nd stimulus. They primarily account for late responses in the train. Even though this model produces plots for var (s_i), var (S_i) and <s_i> plots that are similar to experimental data, it is less attractive than the 2-step model for two reasons. First, the present model assumes an abrupt shift from one set of docking sites to the other. This sudden shift is necessary for the model to work (or else the var (s_i) curve would deviate from the experimental data), but it does not have any simple mechanistic interpretation and is therefore unlikely. Secondly, the present model does not account readily for the latrunculin B/blebbistatin results.

A: Separate var (s_i) plots (circles) and var (S_i) plots (squares) for the two sets of docking sites (red: without replenishment; blue: with replenishment).

B: Simulation of var (s_i) plots (circles) and var (S_i) plots (squares) for the combination of the two sets of docking sites. Some of the var (s_i) points deviate from the N_1= 4 parabola, but overall the var (s_i) curve can be reasonably well fitted with a parabola with N_1= 5.77 (circles and associated continuous parabola). Meanwhile the var (S_i) plot can be approached with a parabola giving N_2= 8.98 (squares and associated dashed parabola). Note similarity with group data of Fig. 5D.

C: <s_i> plot for the same simulation, similar to the experimental results of Fig. 6A.

Supplemental Experimental Procedures

Recording procedures

Sagittal slices (200 μm thick) were prepared from the cerebellar vermis of Sprague Dawley rats (PN 13-16) following the animal care guidelines of our host institution (approval number A-750607). Procedures to record from MLIs were as described (Llano and Gerschenfeld, 1993). About 2/3 of the recordings were from basket cells, defined as MLIs located in the proximal third of the molecular layer, and the remaining 1/3 were stellate cells. This percentage applied both to control data and to data obtained with a pharmacological manipulation (latruncullin B, blebbistatin, or EGTA AM). The composition of the standard extracellular solution was (in mM): 130 NaCl, 2.5 KCl, 26 $NaHCO_3$, 1.3 NaH_2PO_4, 10 glucose, 2 $CaCl_2$, and 1 $MgCl_2$; osmolarity: 300 mosm/l). This solution was equilibrated with 95 % O_2 and 5 % CO_2 (pH 7.4). The standard internal recording solution contained (in mM): 144 K-glutamate, 6 KCl, 4.6 $MgCl_2$, 1 EGTA, 0.1 $CaCl_2$,10 HEPES-K, 4 ATP-Na, 0.4 GTP-Na; pH 7.3; osmolarity: 300 mosm. Alexa 488 was included in this solution to visualize the dendritic tree. Recordings were at 30-34 ^oC.

Extracellular stimulation and recording of single synapses

MLIs were recorded under voltage clamp at -60 mV. After allowing diffusion of the Alexa dye for a few minutes the outline of the dendritic tree was outlined using a CCD camera. For extracellular stimulation a theta-glass pipette was filled with a solution containing (in mM): 145 Na Cl, 2.5 KCl, 2 $CaCl_2$, 1 $MgCl_2$, 10 HEPES-Na, at a pH of 7.3. The extracellular solution was switched to a new solution containing 3 mM external calcium in order to enhance release probability. NMDA receptors and $GABA_A$ receptors were blocked by inclusion of APV (50 μM) and gabazine (15 μM). The tip of the stimulation pipette was positioned on top of a dendrite, at the slice surface. Once a response was found the stimulation threshold was determined, and the position of the pipette was changed to minimize that threshold. During recording, amplitudes of late events were visually inspected, and if these amplitudes appeared heterogeneous, the corresponding stimulation site was abandoned. Definitive acceptance of the experiment as a usable single synapse recording occurred after analysis and depended on 3 criteria (Malagon et al., 2016): (1) a decrement of EPSC amplitudes of second events in a pair, reflecting sharing a common set of receptors belonging to one postsynaptic receptor density; (2) a Gaussian distribution of EPSC amplitudes with a CV less than 0.5; (3) stability of the overall responsiveness over time. PSCs were elicited by voltage steps of 10-30 V (0.1 ms duration). Trains of 8 such pulses (interstimulus interval: 5 ms) were applied repetitively, with intervals of 15 s between trains. Statistical data were derived from sequences of 10-30 trains.

Detection of PSCs during trains

The recorded traces were analyzed using Igor (Wavemetrics, Lake Oswego, USA). Isolated, presumably quantal EPSCs were selected in the late part of the response, aligned with respect to the rising phase, and averaged. The averaged quantal EPSC was fitted with the sum of 3 exponential functions, one for the rising phase and two for the decay. The model quantal EPSC waveform was used to deconvolve the original traces. The deconvolution of the model quantal EPSC was a short transient (called 'spike') and the deconvolution of entire traces were decomposed as the sum of several spikes after adjustment of their amplitudes and times of occurrence. This created a table of evoked EPSCs, each characterized by its time of occurrence and its amplitude. Corrections were applied to account for undetected double EPSCs (estimated temporal separation necessary for detection of individual events, 0.2 ms: Malagon et al., 2016). Temperature plots displayed the estimated numbers of EPSCs for each 5 ms period following individual stimuli, where 'hot' colors feature large vesicle numbers, and failures appear in deep blue (examples in Figs. 1A-B).

Calcium imaging of presynaptic varicosities

Sagittal (200 μm) or transverse (350 μm) slices from rats aged 13 to 15 days were prepared using a modified extracellular saline, as detailed in Brenowitz and Regehr (2007). Experiments were conducted at 32-34 ^oC with the 3 mM extracellular calcium saline used in the electrophysiology experiments. APV (50 μM) and gabazine (15 μM) were included. Granule cells were loaded under whole-cell recording with a solution containing (in mM): 140 K gluconate, 5.4 KCl, 4.1 $MgCl_2$, 9.9 HEPES-K, 0.36 Na-GTP, 3.6 Na-ATP, 500 μM of the calcium-sensitive indicator Oregon green 488 BAPTA-6F (OGB-6F; K_d for calcium of 5.1 μM estimated from *in vitro* calibrations) and 20 μM Alexa-594. Both fluorophores were from Invitrogen. Imaging was performed with a custom-built 2-photon system based on the design of Tan et al. (1999), with 820 nm excitation provided by a MaiTai Ti-Sapphire laser (Spectra Physics, USA). In order to visualize the granule cell axon, large raster scans were performed while acquiring the Alexa 594 fluorescence with a red channel photomultiplier (Hamamatsu H7422 PA-sel, bandpass emission filter 635±65 nm, Chroma Technology). Once a varicosity was identifed, OGB-6F signals were acquired with a green channel (bandpass filtered at 635 ± 65 nm, Chroma Technology; avalanche photodiode Perkin Elmer, SPCM-AQR-13) using raster scans of 5 by 2 µm dimensions at dwell times of 2 ms. The granule cells were kept under current clamp conditions with resting membrane potential around -85 to -95 mV. APs were evoked by 1 ms steps of 350-500 pA. Stimulation protocols alternated between 1, 2, 4 and 8 APs at 200 Hz and were repeated every 20 to 30 seconds. Calcium signaling was analyzed in the pixels encompassing the varicosity in terms of fluorescence changes relative to pre-stimulus values ($\Delta F/F_o$, expressed in %) with software written in the IGOR-Pro programming environment (Wavemetric, Lake Oswego, OR, USA). Averages were performed over 3-11 repetitions.

An 'in vitro' calibration of the dependence of OGB-6F fluorescence on calcium concentration was performed using a series of calcium buffers with high buffering capacity. It gave a ratio of 6.5 between the fluorescence F_{max} at saturating calcium and the fluorescence F_{0Ca} in the absence of calcium, and a K_d of 5 µM. The hyperbolic curve in Fig. 3D (blue trace) corresponds to a linear dependence of the peak calcium concentration Ca_i on AP number assuming $F_{max} / F_{0Ca} = 6.5$, and half saturation following 26 consecutive APs. Ca_i was calculated by inverting the relation $F = F_{OCa} + (F_{max} - F_{OCa})\ Ca_i / (Ca_i + K_d)$ between observed fluorescence and calcium, giving an approximately linear relation on AP number (Fig. 3E). This calculation includes the basal calcium concentration Ca_b as a free parameter. In the figure shown Ca_b was chosen arbitrarily at 50 nM. In practice however, changing Ca_b between 25 and 100 nM did not affect our conclusions, in the sense that the relation between Ca_i and AP number remained linear, with a slope that changed over a small range (0.20 to 0.23 µM/AP). To correct this estimate of Ca_i rise for the added buffering capacity of OGB-6F, we used the relation $Ca_{cor} = Ca_i\ (\kappa_o + \kappa_B)/\ \kappa_o$, where the intrinsic buffering capacity κ_o was taken as 56, and the buffer capacity κ_B was taken as 100 (Brenowitz and Regehr, 2007).

Pharmacological manipulations

Data were collected at least 5 min after switching the bath solution to latruncullin B or to blebbistatin, and 10 min after switching to EGTA-AM.

Monte Carlo simulations

We implemented 5 stochastic synaptic release models based on Monte Carlo simulations using Igor Pro (Wavemetric, Lake Oswego, OR, USA). In all of them, we assumed 4 independent docking sites, which were occupied by synaptic vesicles with a probability of δ before the 1st stimulation. When a vesicle is present at the site, release occurs with a probability of p. In some models, p is a changeable probability that depends on stimulus number (i). After releasing, if replenishment of the docking site is considered, it occurs stochastically with a constant rate R as long as the replacement site is occupied. Simulations proceeded with a time increment of 0.05 ms.

In the cases where a replacement site is assumed to precede the docking site state, occupancy probability of the replacement site is fixed at 1 before starting stimulations. After consumption of the vesicle, replenishment of the replacement site occurs stochastically with constant rate S, if such a replenishment step is considered ("renewable 2-step model").

In each stimulus, we computed the number and cumulative number of released vesicles. And we calculated mean, variance, and covariance for these two sets of parameters. To evaluate the likelihood of various models, we performed least square fits of cumulative variance-mean plots obtained from experimental data. For this fitting model parameters (δ, p, r, s) were incremented with intervals of 0.05.

Statistical evaluation of group results

Results of group data analysis are presented as mean ± s. e. m., or as regression lines. *n* values represent the number of independent experiments. When analyzing means, *p* values are based on Wilcoxon's rank test (either paired or unpaired). When analyzing ratios to control situation, *p* reflects the area of the normal distribution corresponding to the values of the mean and s. e. m. When analyzing correlations illustrated with regression lines, *r* represents Pearson's correlation coefficient, and *p* assesses the probability of correlation given the value of *r* and the number of degrees of freedom of the data.

Supplemental References

Brenowitz, S. D., and Regehr W. G. (2007). Reliability and heterogeneity of calcium signaling at single presynaptic boutons of cerebellar granule cells. J. Neurosci., 27, 7888-7898.

Llano, I., and Gerschenfeld, H. M. (1993). Inhibitory synaptic currents in stellate cells of rat cerebellar slices. J. Physiol. 468, 177-200.

Malagon, G., Miki, T., Llano, I., Neher, E. and Marty, A. (2016). Counting vesicular release events reveals binomial release statistics at single glutamatergic synapses. J. Neurosci. 36, 4010-4025.

Tan, Y. P., Llano, I., Hopt, A., Würrlehausen, F., and Neher, E. (1999). Fast scanning and efficient photodetection in a simple two-photon microscope. J. Neurosci. Methods, 92, 123-135.